POLITECNICO DI TORINO

Corso di Laurea Magistrale in Ingegneria Energetica e Nucleare

Tesi di Laurea Magistrale

Neutronic analysis of the fusion reactor ARC: Monte Carlo simulations with the Serpent code

Relatori
prof. Sandra Dulla
dr. Antonio Froio
ing. Nicolò Abrate

Candidato
Alex Aimetta
matricola: 262772

Anno accademico 2019-2020

Abstract

The fusion reactor ARC proposed by MIT is a concept of high-magnetic field reactor, using high temperature superconductors (HTS), with an innovative liquid breeding blanket (BB) made of a molten salt (FLiBe). The plasma chamber and the vacuum vessel are contained in the liquid breeding blanket and the FLiBe is used also for the cooling of the vacuum vessel and of the divertor. The lithium (isotopically enriched with 90% ^{6}Li) contained in the molten salt has the aim of producing tritium after the interaction with the neutrons produced by the fusion reactions. FLiBe is then extracted from the breeding blanket and sent in a heat exchanger to finally produce electricity with a traditional thermodynamic cycle thanks to the power deposited in the BB by the neutrons and the photons. The designed fusion power of ARC is $525\,\mathrm{MW}$ and its total electric power $283\,\mathrm{MW}$. The presence of high-magnetic field allows to reduce the dimensions of the reactor, with possible benefits on the capital cost.

The aim of this work is to analyze the neutronics of ARC through Monte Carlo simulations using the Serpent transport code. In particular, the simulations are focused on the estimation of the tritium breeding ratio (TBR) and on the distribution of the power deposited by neutrons and photons inside the blanket tank, while the aspects concerning the neutron shielding are not taken into account.

Contents

Chapter 1

Introduction

In the context of the energy production framework, the nuclear fusion energy is expected to have an important role in the long term future.

A fusion reactor is based on fusion reactions that occur in the plasma, which must be confined in order to avoid interactions with the surrounding materials. The most important thing in order to have a working fusion reactor is to confine the plasma. It is possible to have inertial confinement (mostly developed in the USA but which poses proliferation concerns) or magnetic confinement, which is the most common type of confinement used in reactors like ITER, DEMO and ARC.

Fusion is a form of nuclear energy, so a fusion reactor does not produce carbon dioxide during its operating life. Of course, since it is based on nuclear reactions, it is related to radioactive hazards. However, differently from the fission energy source, it is associated to lower levels of radioactivity.

In fact the only products of a fusion reaction, like the most studied deuterium-tritium reaction, are alpha particles and neutrons. This means that the only source of radioactivity is represented by the activation of structural materials after the interaction with neutrons. Of course, there is also the presence of tritium that can be dangerous, but its half-life is of 12.3 years, so it is not an issue on the long scale.

The majority of radioactive wastes from a fusion reactor are low-level and intermediate-level and almost no long-lived and high-level wastes are produced.

Fusion devices are not based on chain-reactions like fission reactors, so they are not affected by criticality issues and this avoid to have accidents related to the divergence of the power. In this sense a fusion reactor is intrinsically safe. In fact, when the plasma becomes uncontrollable in a fusion reactor, the fusion reactions automatically stop.

Moreover, after the shutdown, the residual heat derives mainly by the decay of activated materials in the structural components of the reactor, and not by the decay of fission products. Therefore, the removal of the residual heat in a fusion reactor is easier than a fission one.

All these aspects related to the safety of fusion reactors make them particularly attractive if compared to fission reactors, which are generally considered as dangerous devices for the energy production by the public opinion.

Fusion reactions are characterized by a higher energy production density than fission reactions, because the fuel is made of light isotopes like deuterium and tritium. The result is that the fuel mass necessary in a fusion reactor is much lower than the uranium fuel in a fission device with the same power.

This is particularly important since the tritium is not present in nature because of its short half-life. Therefore, it is important that the amount of tritium required for the start up and the steady-state operational phase of a fusion reactor is limited. Since tritium is not present in nature we need artificial techniques in order to produce it. Limited quantities of tritium are produced in fission reactors, in particular in CANDU reactors, but they are not sufficient for large scale fusion power production.

For what concerns deuterium, there are not particular issues related to the available quantity, since it is estimated that in the seawater there are about 4.5×10^{-13} t of deuterium.

The best solution to artificially produce tritium currently is to surround the plasma chamber and the vacuum vessel with a breeding blanket composed by materials like lithium which is able to produce an atom of tritium after the interaction with a neutron. In this way it is hypothetically possible to produce an atom of tritium inside the blanket per each burned tritium inside the plasma. There is a particular quantity that describes this phenomenon and it is called tritium breeding ratio (TBR) and in the previous situation TBR is equal to unity.

Real reactors are not made only by breeding materials, but also by structural ones and if the neutrons are absorbed in the latter and don't interact with the lithium, they are lost in the sense that they don't contribute to the production of tritium. This aspect leads to an actual TBR<1.

Moreover, it is possible that some of the tritium produced gets lost inside the systems present in the fusion plant for its extraction from the breeding blanket and re-injection inside the plasma. For this reason it is not only important to achieve a TBR=1, but also a TBR>1 in order to compensate the tritium that can be lost inside the reactor.

A possible way to obtain a TBR>1 is to use some materials that work as neutron multipliers, like beryllium, in order to compensate the neutrons absorbed in the structural components, and to enrich the lithium with its isotope ^{6}Li because its tritium-production cross section with neutrons is not zero for all the neutron energies, while ^{7}Li is characterized by a threshold behavior.

Moreover, having a TBR>1 is also necessary in order to produce the tritium necessary for the start-up of another reactor, so that fusion reactors can actually become a commercial technology.

According to these considerations it is clear how much important is the evaluation of the TBR in the modelling of a fusion reactor.

Similarly to fission reactors, also in fusion reactors the energy is obtained by nuclear reactions but then this energy is converted in heat power in a operating fluid which is then sent in the balance of plant for the production of electrical power following a traditional thermodynamic cycle. This is another key aspect in the modelling of a fusion reactor, if we want it to produce electrical power.

In general the fluid used in fission reactors is water. Traditional fusion reactor designs, like ITER, uses water too. The main limitation of water inside a fusion reactor is that it can work only as a coolant, while for example in a thermal fission reactor it works also as a moderator. Therefore, it does not seem that water can be the smartest choice as operating fluid in fusion devices.

A possible solution in this sense is to use a fluid which is able at the same time to serve as coolant, breeder and shielding for the neutrons. A fluid of this type is the FLiBe, a molten salt composed of fluorine, beryllium and lithium. FLiBe allows to reduce the amount of different materials inside the reactor and allows to substitute the traditional solid breeding blanket with a liquid breeding blanket, reducing the amount of structural material too. In this way the issues related to radiation damage and activation of structural materials are partly mitigated.

The use of a fluid breeding blanket is one of the main innovation in the design of the Affordable, Robust, Compact (ARC) fusion reactor developed at MIT [1].

The second important innovation of ARC is the presence of high temperature superconductive (HTS) materials for the confinement of the plasma, allowing to achieve higher magnetic fields and to reduce the volume of the reactor keeping the fusion power similar to bigger designs like ITER.

The electrical output of ARC ($200\,\mathrm{MWe}$) is much smaller than other fusion concepts like ARIES ($1000\,\mathrm{MWe}$). This is not necessarily a drawback, indeed the construction of a smaller reactor will have benefits from the economics point of view. Moreover it could lead to the development of an energy grid composed of many smaller reactors localized in different regions of the world, instead of the large scale fission reactors currently present.

The main reason for which there are still not any operating fusion rectors able to magnetically confine the plasma for long times and to produce electrical power is related to technological issues. In fact there are not known materials able to sustain the huge heat fluxes produced by the fusion reactions inside the plasma chamber, in particular in the divertor region.

Some possible solutions could be to use liquid metal divertors instead of solid ones, to intervene on the plasma physics in order to obtain the plasma detachment or to design advanced, double-null, long-legged divertor. The latter solution is proposed in the design of ARC.

Another issue of many fusion reactor designs (like ITER and DEMO) is that the plasma confinement and, in particular, the generation of the plasma current necessary for the confinement, are obtained in an inductive way with the transformer principle. This means that the power production cannot be continuous but has a pulsated behavior, limiting the possibility to use fusion reactors as base loads power plants.

ARC tries to overcome this problem with an inboard launched lower hybrid current drive (LHCD) that allows to generate the plasma current in a non-inductive way.

1.1 Aim of the work

In any type of fusion reactor, there are many aspects to consider in the framework of the modelling. These are mainly the plasma physics, the divertor heat flux challenge, the neutronics and the magnet design.

This work is focused on the neutronics of the fusion reactor ARC that, even if can be considered a small reactor compared to other fusion reactors (like ITER and DEMO), is characterized by large dimensions.

The study is performed using Serpent, a Monte Carlo transport code. Serpent was initially developed for fission systems, so this is also an opportunity to evaluate if it is suitable even for nuclear fusion devices and to find out which aspects have to be modified in the code in order to improve it for fusion applications.

Due to the large dimensions of ARC, the work is not focused on the whole design but only on the modelling of the TBR and the power deposited inside the breeding blanket tank by the neutrons produced by D-T fusion reactors, also considering the crucial importance of these two quantities in the context of a fusion reactor.

The TBR and the power deposition are interesting for what concerns the fuel self-sufficiency of the reactor, the power production and also the evaluation of the thermo-mechanical integrity of the structural components.

The design of ARC is presented in chapter 2.

The principle of the Monte Carlo modelling are described in section 3.1 and the main features of the Serpent code in section 3.2.

The rest of the thesis is organized with the description of how the geometry model of ARC was obtained (section 3.3), a section where it is explained how the external neutron source was defined (section 3.4) and another one which explains the rationale used for the definition of the detectors (section 3.5) for the evaluation of reaction rate densities to obtain information about the TBR and the power deposition.

Finally, the result of the Serpent simulations are presented in chapter 4 which is divided in a first section (4.1) with the results obtained using a spatially uniform neutron source and a second section with a more realistic source (section 4.2) which takes into account that the production of neutrons is higher in the central region of the plasma chamber.

Chapter 2

The ARC reactor

2.1 Design motivation and overview

The affordable, robust, compact (ARC) reactor [1] (fig. 2.1) is an innovative conceptual design based on the tokamak concept developed by Massachusets Institute of Technology researchers with the aim of reducing the size, cost and complexity of traditional designs of nuclear fusion reactors.

Most of the fusion reactors (like DEMO and ARIES studies) for the production of electricity are designed to produce output power in the order of $1\ \mathrm{GWe}$. A design of this type is related to high cost and long construction time and as a consequence the implications of possible failures during the development of the design could be dramatic.

Instead, the ARC reactor, with $200\ \mathrm{MWe}$ of output power, is a lower risk alternative. It is a high magnetic field design using REBCO (rare-earth barium copper oxide) high temperature superconducting (HTS) tapes and inboard lower hybrid current drive (LHCD) to generate the plasma current in a non-inductive way.

One of the main issues related to nuclear reactors is the capital cost and the related financial effort, that is often an obstacle for the realization of reactor themselves. ARC tries to reduce the capital cost in the most intuitive way: minimizing the reactor size.

However, a solution of this way is not trivial, since reducing the size means that the coils are nearer to the source of neutrons, with possible consequences on the shielding; in addition a smaller volume is associated to a higher power density $[\mathrm{MW/m^3}]$, which can be an issue from the safety point of view.

The ARC reactor has a higher surface to volume ratio thanks to the shorter major radius and the result is that the global heat flux $[\mathrm{MW/m^2}]$ of ARC is similar to larger reactors. In this way, the capital cost is reduced thanks to the smaller volume, without compromising the performances of materials with too high heat fluxes.

ARC is based on a deuterium-tritium plasma, as the more traditional designs, with a relatively small fusion power (around $500\ \mathrm{MW}$), similar to the fusion power of ITER which, however, is not designed for the production of electrical power.

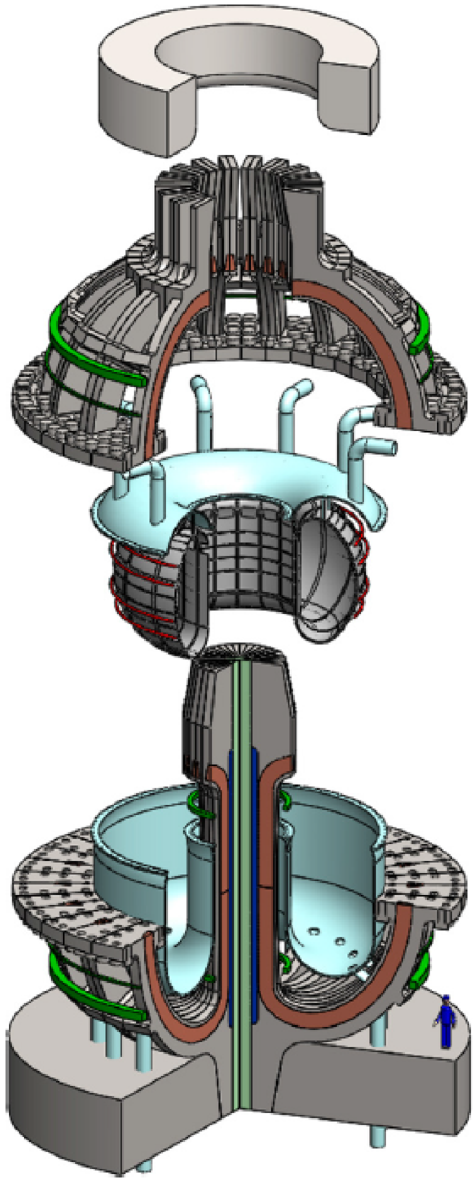

Figure 2.1: Exploded view of ARC. The dimension of the reactor can be compared with the man in blue [1]

The idea is to combine the small size of ARC with the high magnetic fields obtained with HTS magnets. In fact a fundamental equation for the design of any magnetic fusion concept is:

$$P_f \propto \beta^2 B_0^4 V_p. \tag{2.1}$$

Since the volume of the plasma (V_p) is reduced and the value of the pressure ratio

(β) can not be too high in order to avoid instabilities inside the plasma, the best solution seems to be increasing the magnetic field at the magnetic axis of the plasma (B_0).

Increasing the magnetic field is an issue from the point of view of the technology, in fact in many of the fusion reactor designs (for example ITER and DEMO) the magnetic field is generated by low temperature superconductive materials that lose superconductive properties when the generated magnetic field is too high. For this reason if the aim is to increase the fusion power increasing the magnetic field, the best solution is to use high temperature superconductive materials like REBCO tapes, characterized by high critical current density at high magnetic fields.

A direct benefit of HTS materials can be understood considering that the inboard space for the toroidal coils is limited. So, if LTS are used, a large amount of this space should be occupied by superconducting materials (because of the drop of the critical current of LTS at high magnetic fields) in order to achieve higher magnetic fields. The result is huge Lorentz forces that acts on a small volume of structural material increasing the overall stress on the structure.

Using HTS, a lower amount of superconducting materials is needed in order to obtain the same magnetic fields and so a larger volume can be occupied by structural material.

The main drawback of HTS is that at the state of the art they are underdeveloped compared to low temperature superconductive materials and there are still many issues related to cost, mechanics, quench and anisotropy. However the possible advantages are so attractive that research in HTS is currently a main topic in the nuclear fusion field. In this sense, ARC will be an important test bench.

Another advantage with REBCO tapes is the possibility to use resistive joints in the coils (thanks to the higher temperature, which can enable also the use of different coolant like liquid hydrogen or liquid neon instead of liquid helium proposed for LTS magnets in ITER and DEMO), so that the toroidal field coils can be separated in two pieces with dramatic consequences on the maintainability, enabling to easily replace temporary components like the blanket tank, the vessel, the auxiliary and poloidal field coils.

Modular maintainability and replacement are also allowed by the improved thermal properties obtained thanks to the higher operating temperature window, guaranteed by the use of REBCO tapes, around $20\,\mathrm{K}$ and $30\,\mathrm{K}$ (while Nb_3Sn used in ITER can work only up to $4\,\mathrm{K}$). Maintainability and construction simplicity are two key aspect in the design of ARC and can speed up its development on the industrial scale. Finally, REBCO tapes are also easier to fabricate than LTS like Nb_3Sn.

According to the design of ARC, the plasma energy gain (defined as the ratio of fusion power produced to the power required to maintain the plasma) is larger than 10, which is the design value of ITER. It is obtained in a smaller volume with a major radius of $3.3\,\mathrm{m}$ ($6.2\,\mathrm{m}$ for ITER) and a minor radius of $1.1\,\mathrm{m}$ thanks to the presence of high temperature superconducting REBCO tapes which allows to reach a peak magnetic field on the coil around $23\,\mathrm{T}$ and of $9.2\,\mathrm{T}$ on the plasma axis ($11.8\,\mathrm{T}$ and $5.3\,\mathrm{T}$ respectively in ITER).

A parameter similar to ITER is the fusion power, around $500\,\mathrm{MW}$ in steady state. This power is produced in a volume eight times smaller than the one of ITER, with possible consequences on the plasma power exhaust.

Other significant parameters for ARC are the plasma current of $7.8\,\mathrm{MA}$, the average plasma temperature of $14\,\mathrm{keV}$, the average plasma density of $1.3 \times 10^{-20}\,\mathrm{neutrons/m^3}$.

The previous parameters are similar to other reactors with the same fusion power like ITER, the big difference of ARC is related to its smaller volume and higher magnetic field.

2.2 The vacuum vessel and the FLiBe blanket

The plasma chamber of ARC is put inside a single-piece and replaceable double wall vacuum vessel made of Inconel 718, a nichel-based alloy, chosen due to its high strength and corrosion resistance at elevated temperature, even if it is extremely prone to nuclear activation because of the presence of nichel.

Therefore, Inconel 718 is probably not the material that will be used in the final design, but other materials like Eurofer97 and V-15Cr-5Ti will be tested too. This is a peculiar characteristic of ARC, since its design is continuously evolving and it is open to new ideas and technology, until the construction will be committed [2].

The vacuum vessel is located in a region with high thermo-mechanical loads and neutron fluxes and can be subjected to plasma disruptions, so it is an independent component that can be replaced without consequences on the permanent components.

Moreover, it would be interesting to obtain a load-following power plant changing the fusion power in time. A plant of this type is characterized by cyclic thermal loads and neutron fluxes, which can affect the performances and the integrity of the vacuum vessel. Therefore, it is important to evaluate the lifetime of this component [2].

The double-vessel contains a cooling channel where single-phase FLiBe molten salt poloidally flows for the active cooling of the vessel itself and for the breeding of tritium. It contributes also to the neutron shielding of the outer vacuum vessel.

Eighteen support columns attach the vacuum vessel to the blanket tank and contain components like waveguides and vacuum ports important for the communication with the external world.

In order to make full use of the maintainability scheme allowed by demountable TF coils, the blanket is completely composed of continuously recycled liquid FLiBe which plays the role of neutron moderator, breeder, shield and neutron multiplier. Moreover, the FLiBe works also as tritium carrier, with the tritium extracted from the liquid FLiBe after it flows out of the blanket tank [1].

This is an important innovation since only one material is used for four different functions. It is put in a single-piece low-pressure blanket tank, made of Inconel 718, which acts as the primary nuclear containment boundary.

Even if at low pressure, the FLiBe is a high-temperature single phase fluid (between 732 K and 1700 K), so that it is also an efficient thermal reservoir, minimizing safety issues related to two-phase operating fluids.

The neutrons produced by the D-T reaction pass through the thin double vacuum vessel and reach the blanket where they deposit their energy later extracted from the blanket and converted in electric power in the balance of the plant, and interact with lithium breeding tritium, necessary for the self sufficiency of the reactor.

FLiBe is not only the most suitable liquid salt for the moderation, breeding and shielding, but it is also a smart choice in this case because it has a low electrical conductivity and since in ARC the magnetic field is higher than in ITER or DEMO, this property extremely reduces the magneto hydrodynamics effects in the flow. Having low MHD effects, means the possibility to achieve sufficient fluid flow with low pressure drop and pumping power.

The presence of a large blanket tank is also an advantage because simplifies the geometry of the reactor and prevents the issues related to cyclic loads, since it eliminates a big amount of structural and solid materials which would be affected by fatigue and reduces the amount of radioactive waste too. The only exception to the FLiBE inside the blanket is represented by the eighteen support columns. A poloidal section of the vacuum vessel and blanket tank inside the TF coils is shown in fig. 2.2.

In the initial design, a neutron shield made of titanium dihydride around the blanket tank was proposed, for the protection of the superconducting coils, but then it has been substituted by zirconium hydride plates inside the blanket tank at the location of the poloidal coils. This is also possible thanks to the shielding effect performed by the thick FLiBe blanket.

The role of neutron shielding inside a small fusion reactor is probably even more important than large scale reactors and it is able to affect the operational lifetime of the superconducting coils. The result is that the maintenance of the coils is reduced as well as the cost of superconductive materials in case of substitution (its important to remember that the coils are the most expensive components inside a fusion reactor and with HTS materials they are even more expensive).

2.3 The divertor

ARC is based on a divertor configuration. The presence of a divertor is important for the performances of the plasma, for example it contributes to the stability and reduces the amount of impurities inside the plasma itself, avoiding plasma-wall interactions.

The main challenge of a divertor configuration is that the heat flux that must be exhausted by the divertor plates is huge. Considering a fusion power of 525 MW, around 105 MW are associated to charged alpha particles which are entrained by the magnetic field and must be exhausted by the divertor plates. The surface where

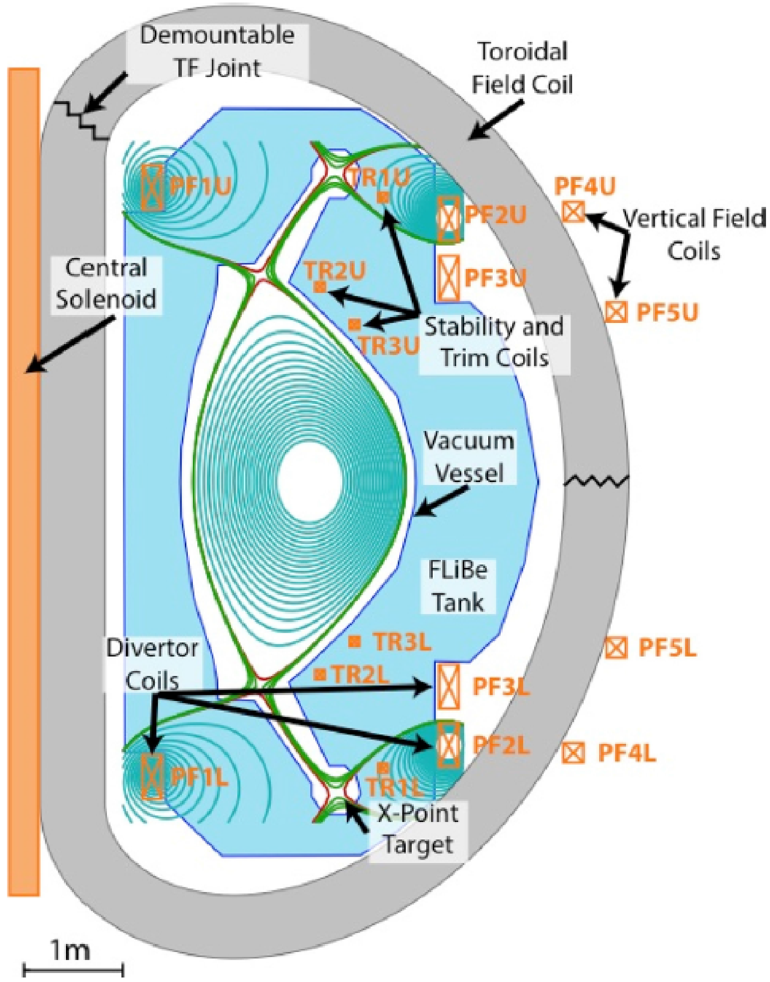

Figure 2.2: Poloidal section of ARC [3]

this power must be exhausted is related to the scrape-off layer thickness and, in general, for a power reactor it can be approximated to a circle of radius 1 mm.

The final result of this situation is a heat flux higher than $10\,\mathrm{MW/m^2}$, which can not be sustained in steady state for long time by known materials.

A possible solution is to design advanced divertor geometries with extended volumes for the divertor and additional poloidal field nulls. These types of advanced divertors generally need an extremely precise control performed by the poloidal coils.

In many reactors (like ITER and DEMO) the TF coils are not demountable and so the PF coils must be placed outside for practical consideration. In this way the PF coils are far from the plasma and in order to control the shape of the plasma they need to carry huge currents and, as a consequence, to sustain huge Lorentz forces.

In the case of ARC the TF coils are demountable, so the PF coils can be put inside them nearer to the plasma, with the possibility to reduce the current in the coils.

The presence of the thick FLiBe blanket reduces the neutron flux at the poloidal coils, which otherwise would be subjected to too high neutron fluxes since they are near to the neutron source.

Another benefit resulting from the presence of the big breeding blanket is that it is possible to implement an advanced, long-legged divertor extracting the adequate space in the blanket itself, with no need to reduce the plasma volume or increase the TF coil dimensions.

The previous configuration, proposed for ARC in [3], has the divertor cooled by FLiBe.

A recent study by Umansky et al. [4] has demonstrated that a configuration of this type can generate a stable and fully detached divertor (which is the only solution if more complex design like liquid metal divertor are not used) able to exhaust heat fluxes ten times larger than traditional divertor with minimal levels of impurity seeding.

In conclusion, according to Eich scaling [5] and detailed study by Reinke [6] the presence of high magnetic field coupled with small dimensions typical of ARC neither simplifies nor complicates the power exhaust challenge with respect to traditional reactors with smaller field. So, again, ARC design is mainly an advantage from the point of view of the capital cost. The divertor design of ARC is represented in fig. 2.2.

A key aspect of the divertor design is the design of the target plates. They are similar to ITER's targets, with a plasma-facing surface made of tungsten, embedded cooling channels and a structural substrate made of another material. The coolant inside the cooling channels is not high-pressure water but high-temperature single-phase FLiBe.

The divertor also benefits of the vertical maintenance scheme of ARC that allows to replace the entire assembly and reduces the need of remote maintenance inside the vacuum vessel.

Thanks to the particular design of the long divertor leg, the estimated heat flux on the divertor surface is $1.4\,\mathrm{MW/m^2}$ even if the design specification is $12\,\mathrm{MW/m^2}$ due to the uncertainty on the heat flux and to have a larger safety margin.

The use of FLiBe introduces problems of corrosion in the divertor, so a trade-off between the maximum thickness related to the heat deposition and the minimum thickness related to corrosion issues must be found. There are some experimental data of corrosion rates of static FLiBe on Inconel which say that the corrosion rate is in the order of $\mu\mathrm{m/year}$, but further studies with flowing FLiBe must be performed.

The proposed design is a $3\,\mathrm{mm}$ of solid tungsten actively cooled by $2\,\mathrm{m/s}$ flowing FLiBe and a $4\,\mathrm{cm}$ Inconel 718 backbone for structural support, proved to be capable of exhausting an incident heat flux of $12\,\mathrm{MW/m^2}$. A sketch of ARC's divertor target plate is shown in fig. 2.3.

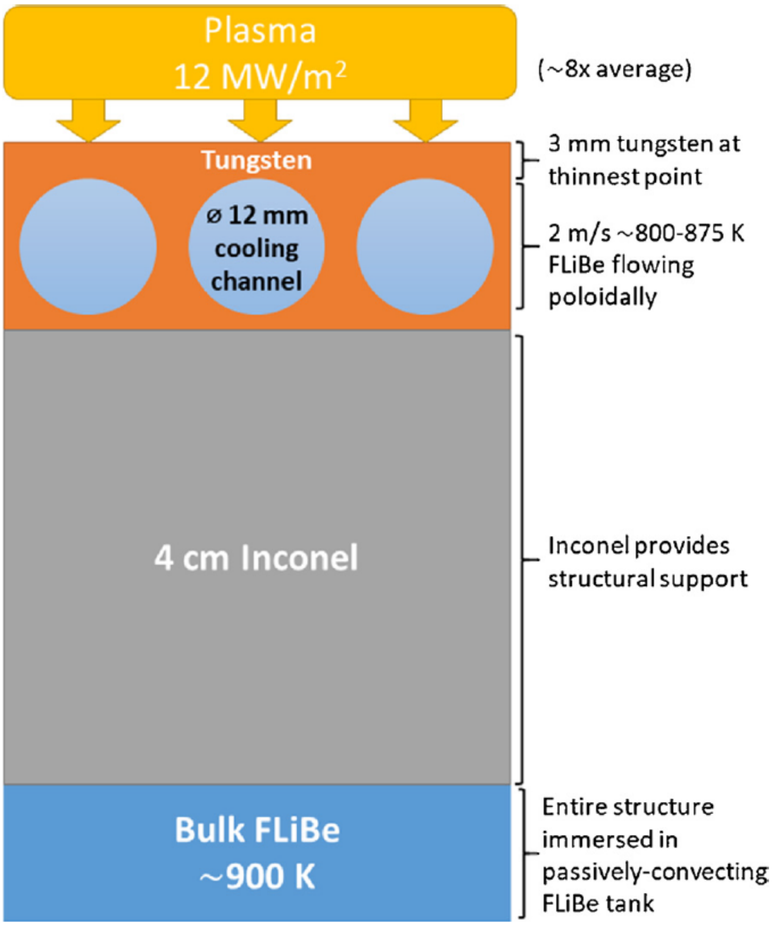

Figure 2.3: Cross-section of divertor material layering. [3]

2.4 Magnet design

The design of the ARC magnet system considers REBCO tapes for toroidal fields, central solenoid and poloidal field coils and copper for the low-current auxiliary coils located inside the blanket near to the plasma.

TF coils and PF coils are steady state superconducting magnets for stability, shaping and startup of the plasma. The conductor used to produce the magnetic field is mostly composed of copper and Hastelloy, with a thin layer of REBCO superconductor operated at $20\,\mathrm{K}$ (fig. 2.4). In this sense it is "sub-cooled", because its operating temperature is much lower than the critical one ($80\,\mathrm{K}$).

However, having a higher temperature margin as in this case could be an issue in case of quench, with a large amount of energy concentrated at the location of the quench itself without energy propagation in the coil. On the other hand, with a higher temperature margin it is more difficult to have a quench.

The amount of superconducting material is chosen so that the current density is

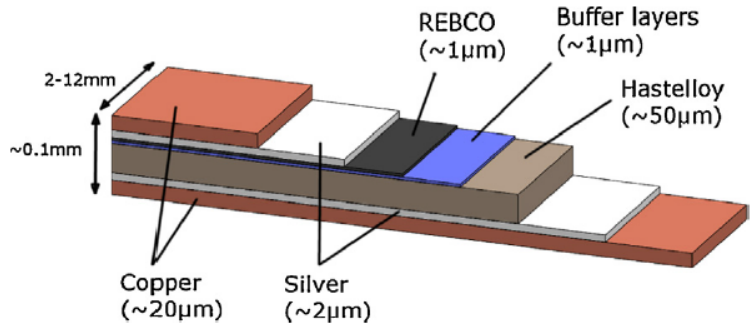

Figure 2.4: Schematic, not to scale, view of the cross section of REBCO tape superconductor by SuperPower Inc. [1]

always lower than the 50% of the critical value and the amount of copper guarantees that the temperature of the conductor during a quench stays below $200\,\mathrm{K}$.

Thanks to the higher temperature allowed by the use of HTS, the magnet cooling in ARC is performed by liquid hydrogen, due to its abundance and low cost compared to liquid helium. Other benefits associated to the higher temperature are the reduced thermodynamic cost of the cooling and the enhanced thermal stability thanks to the higher heat capacity.

The 18 toroidal field coils have the typical D shape structure, demonstrated to be the best in order to minimize the mechanical stress, made of cryogenic 316 LN stainless steel to support the huge Lorentz forces. They are composed by a removable upper part and a fixed lower leg, allowing demountablity.

Each of them carries a current of $8.4\,\mathrm{MA}$, carried by 120 superconducting cables, each with $70\,\mathrm{kA}$ flowing. Each of the 120 cables consists of $12\,\mathrm{mm}$ wide, $0.1\,\mathrm{mm}$ thin REBCO tapes built in a copper stabilizer surrounded by a $40\,\mathrm{mm} \times 40\,\mathrm{mm}$ square steel jacket, the so called cable-in-conduit conductor (CICC) technique. The total length of REBCO tapes in each TF coil is about $5730\,\mathrm{km}$ but the length of each REBCO tape is $17\,\mathrm{m}$ in the bottom leg and $7\,\mathrm{m}$ in the top one. This is an incredible improvement compared to the continuous coil winding of ITER.

The central solenoid is mainly used for inductive startup of the plasma current and for off-normal plasma current control, while in steady state operation the plasma current is generated non-inductively by lower hybrid current drive (LHCD). It is layer-wound with REBCO CICC cables, similarly to TF coils, and operates between $-63\,\mathrm{MA/turn}$ to $63\,\mathrm{MA/turn}$, with a peak field on the coil of $12.9\,\mathrm{T}$ similarly to ITER.

The fact that the central solenoid will not be used during steady-state operation and its functioning is limited to a small number of cycles, reduces the related fatigue concerns compared to ITER where it is continuously subjected to transient stresses.

The PF coils are used to generate the X-points inside the plasma and are located outside the blanket tank but inside the TF coils. They don't need joints since the demountability of TF coils permit to easily extract and insert them. The PF coils are shielded both by the FLiBe blanket and by neutron shields made of zirconium hydride. There is also a set of poloidal coils for outboard plasma shaping and equilibrium fields outside TF coils.

The auxiliary coils are located inside the blanket and near the plasma because their aim is to control in real-time the shape of the plasma, helping to avoid disruptions. They are subjected to intense neutron flux, for this reason they are made by copper and not by superconducting materials.

The other reason for which they are made by copper is that they carry a lower current in the order of some kA, thanks to the fact that they are near to the plasma and so the magnetic field can be less intense. Their section has a radius of $5\,\mathrm{cm}$, so they have a very little effect on the neutronics of the reactor.

Since ARC is based on HTS which can work at higher temperatures, the fluid used for the magnet cooling is liquid hydrogen pressurized between $5\,\mathrm{bar}$ and $10\,\mathrm{bar}$ to increase the liquid temperature range. The cooling circuit of TF coil is located inside the copper stabilizer, while the joints are cooled by channels inside their honey-comb structure. The two circuits are independent.

The heat from the $900\,\mathrm{K}$ FLiBe blanket is removed at different stages before reaching the TF coils: the thermal shielding and the neutron shielding that surrounds it, and it's separated by the TF coils by three vacuum gaps, cooled by liquid water, while the the thermal shield of the first gap is cooled by liquid nitrogen and the outer one by liquid hydrogen. The water loop removes MW of heat, while the nitrogen loop and hydrogen loop remove a lower amount of power (in the order of several kW) at a lower temperature.

Globally, the electrical power required for the pumping of this circuits is around $5.1\,\mathrm{MW}$, negligible if compared to the dimension of the reactor, to remove $2.1\,\mathrm{MW}$ of heat power. The auxiliary coils inside the blanket are cooled with FLiBe.

2.5 Economics

One of the main driver for the development of the ARC reactor is the theorically lower cost due to the smaller size of the reactor. However, it will use some extremely expensive materials like in the HTS, so it is important to analyse if ARC is actually feasible from the economical point of view.

The first analysis of this type was presented in [1] and it did no consider the divertor since at the time when the article was published the design of the divertor was still an open question.

The analysis estimates a cost of $92.7M of fabricated material for the replaceable vacuum vessel (considering that in the initial design the thickness of the tungsten was 2 cm, while now it is 1 mm, so we can expect the cost is even lower now).

Concerning the blanket, the analysis considers the blanket tank, the TiH_2 shield, the FLiBe channel, the FLiBe blanket and the FLiBe heat exchanger. In this case the material cost of FLiBe and TiH_2 is equal to the fabricated cost because the two materials are, respectively, in liquid and powder form. The total cost of the blanket is expected to be $257.2M.

Finally, the magnets (magnet structure, magnet top ring, REBCO structure and REBCO tape) cost is in the order of $5.1-5.2B, with the largest contribution given by the fabrication of the magnet structure ($4.6B of fabricated cost against the $42M of the material cost).

The total cost of the materials for ARC is of $430M assuming the highest cost estimate for the REBCO tapes and the total fabricated cost is $5.5-5.6B (see table 2.1).

Table 2.1: Cost for ARC reactor

	Material cost	Fabricated cost
Replaceable VV	$5.5M	$92M
Blanket	$160M	$260M
Magnets	$160-260M	$5.1-5.2B
Total	$330-430M	$5.5-5.6B

It is clear how the cost of the materials is only a small fraction of the final cost, so we can expect that if the design of ARC will become commercial the fabricated cost will reduce thanks to the economy of scale, in particular for what concerns the fabrication of the magnets. The final cost of ARC is dramatically lower than the cost of ITER ($24B), even if both have the same fusion power and ARC produces net electricity.

Chapter 3

Monte Carlo Modelling of the ARC reactor

3.1 Monte Carlo Modelling

Neutron transport theory studies the propagation of neutrons inside media and all the related phenomena (e.g. transmutation, activation, radiation damage and so on). Solutions of the neutron transport equation can be addressed with both deterministic and stochastic numerical techniques.

The deterministic approach consists in a series of equations that describes the system of interest. In general these equations can not be solved analytically, therefore it is necessary to discretise space, energy, direction and time.

Several methods like the method of characteristics, the spherical harmonics method and the discrete ordinate method have been developed during the last fifty years in order to solve the transport equation with great accuracy. In any case, the result is an approximated solution.

The advantage of the deterministic approach is that once the transport equation is solved, this is the final result and can be used as a first approximation of the nuclear device.

The second approach is based on probability and statistical theories: the so called Monte Carlo method. It describes accurately the propagation of randomly moving neutrons without, in principle, any approximations. It can be used also for more complex geometries and its results are generally more accurate than the ones of a deterministic method.

The main drawback of the Monte Carlo method is that it does not give a quick approximated solution of the transport equation. This is because the Monte Carlo method is a probabilistic approach based on the convergence of stochastic results to a mean value. If we want a result with a low statistical error, we need a large amount of simulations that require a remarkable amount of computational effort. Another issue of the Monte Carlo method is its slow convergence rate as $1/\sqrt{\mathrm{N}}$ [7], where N is the number of experiments performed.

The Monte Carlo method is becoming more and more popular thanks to the development of new powerful computers able to reduce the computational time to perform the adequate number of simulations.

In this work the modelling of the ARC reactor is performed using the Monte Carlo method.

3.1.1 Basic principles of the Monte Carlo method

The Monte Carlo method is based on random sampling processes, where the sampling is performed according to specific probability laws. After this step it is possible to collect statistical data from the samples and use them to infer information about the particles (in this case neutrons) population.

It is a set of numerical statistical methods with the objective to evaluate average values of random variables in statistical systems, to simulate complex systems knowing their basic physics phenomena. The result of the simulations are presented in terms of expected values of the random variable distributions.

The fundamental mathematical theory of the Monte Carlo method is probability. All stochastic phenomena that occur in reality are transformed in analogue events that can be described in terms of probability.

Once we have a basic event, it is possible to define random variables in order to have a better mathematical definition of the problem. In fact, if we think to the simple case of a coin, the two possible events are heads or tails. It is not easy to manage two events of this type in a mathematical manner. For this reason we introduce a random variable in order to assign to each of this two event a number.

The main implication of the random variable definition is that we are considering no more the probability of an event but the probability of numbers associated to it. In this way the probability becomes a real function.

Once the random variable is introduced, it is possible to define the cumulative density function (CDF): the CDF of a variable x is the probability that the outcome of an experiment in terms of the random variable ξ is lower or equal than x. In mathematical form:

$$F_\xi(x) = P[\xi \leq x]. \tag{3.1}$$

This function can be used to describe the statistical phenomenon and its events in terms of probability.

The probability density function (PDF) $f_\xi(x)$ is another function which gives the probability in the neighborhood of x of the outcome of an experiment in terms of the random variable ξ .

The PDF is the derivative of a CDF, if the CDF is continuous and derivable. If we know the CDF or the PDF of a statistical phenomenon, it is possible to get average information about it.

In general, random phenomena are described in terms of PDF. For example the radioactive decay and the free flight of a particle are associated to an exponential

PDF.

In order to obtain average information about the statistical phenomenon it is necessary to define the concept of n-th order moment:

$$E[x^n] = \int_{-\infty}^{+\infty} x^n f_\xi(x)\, dx. \tag{3.2}$$

If n=1, the result of the integral is the mean value:

$$E[x] = \int_{-\infty}^{+\infty} x f_\xi(x)\, dx. \tag{3.3}$$

Another fundamental quantity is the variance (the mean quadratic error):

$$\sigma^2[x] = \int_{-\infty}^{+\infty} (x - E[x])^2 f_\xi(x)\, dx = E[(x - E[x])^2]. \tag{3.4}$$

Finally, the square root of the variance is the so called standard deviation:

$$\sigma[x] = \sqrt{\sigma^2} = \sqrt{E[(x - E[x])^2]} \tag{3.5}$$

and the relative standard deviation is defined as:

$$RSD = \frac{\sigma}{E[x]} \tag{3.6}$$

If we perform N experiments, each of them is associated with a corresponding value of the random variable ξ_i. All the values of ξ_i of a certain experiment are random numbers, identically distributed (according to the same PDF) and are statistically independent.

It is now possible to define a new random number called sample average:

$$\bar{\xi}^N = \frac{1}{N} \sum_{i=1}^{N} \xi_i. \tag{3.7}$$

The mean value and variance of the sample average are:

$$E[\bar{\xi}^N] = E[x] = \mu \tag{3.8}$$

$$\sigma^2[\bar{\xi}^N] = \frac{\sigma^2[x]}{N}. \tag{3.9}$$

The results of (3.8) and (3.9) are important because they say that the random number $E[\bar{\xi}^N]$ is an estimator of the expected value and its dispersion with respect to the mean value is described by $\sigma^2[\bar{\xi}^N]$. Increasing the number of experiments, the dispersion decreases.

The mathematical foundation of the Monte Carlo method lies in two theorems. The first one is the Tchebycheff inequality applied to the sample average:

$$P[|\bar{\xi}^N - \mu| > k] \le \frac{\sigma^2}{Nk^2} \tag{3.10}$$

which says that, increasing the number of experiments N, the sample average converges in probability to the mean value μ.

This information is useful but not sufficient because it does not say which is the difference between the value of the sample average and the mean value at a given number of experiments. This type of information is given by the central limit theorem (CLT): if $N \to \infty$, then $\bar{\xi}^N$ has a normal distribution.

Thanks to the CLT it is possible to obtain, with some algebra, that:

$$P\left[\left|\frac{\bar{\xi}^N - \mu}{\bar{\xi}^N}\right| \leq \frac{\sigma}{\sqrt{N}|\bar{\xi}^N|}k\right] = \begin{cases} 0.68 & \text{if } k = 1 \\ 0.95 & \text{if } k = 2 \\ 0.99 & \text{if } k = 3 \end{cases} \tag{3.11}$$

which means that the probability that the relative error of the sample average is lower than k times the relative standard deviation of the sample average has a precise value. It is not possible to perform $N \to \infty$ experiments using a computer, so the result of the CLT is approximated for "N that tends to a high number of experiments".

In this way it is possible to obtain the statistical error bars associated to the results of the Monte Carlo simulations. For example, if k=1, it means that there is a probability of 0.68 that the expected value is inside the error bar. Another information given by the CLT is that the convergence rate goes as $1/\sqrt{N}$.

This is the theory at the base of the Monte Carlo method. Then, we need some techniques in order to sample random numbers according to the CDF of the problem (e.g. the inverse transform method) or to the PDF (e.g. the rejection method).

Finally, for what concerns the neutron transport, it is fundamental to define the concept of random walk. A random walk is a mathematical object that represents a random path in a certain space that follows a statistical law. It is possible, for example, to evaluate how many neutrons pass through a certain state or count where a neutron is absorbed, all in terms of probability.

Therefore, information about the PDF for the generation of a neutron, about the PDFs that governs the propagation of neutrons in terms of direction (isotropic or non-isotropic) and of free flight and finally about the PDF of a collision, in order to know what is the probability that a neutron is absorbed compared to all the other phenomena that can occur after a collision, is needed.

All these phenomena are represented in terms of probability, so it is possible to use a Monte Carlo approach for the evaluation of the neutron transport.

3.2 The Serpent Monte Carlo code

Serpent is a multi-purpose, three-dimensional, continuous-energy Monte Carlo particle transport code, developed at VTT Technical Research Centre of Finland, Ltd. The development started in 2004, and the code has been publicly distributed by the OECD/NEA Data Bank and RSICC since 2009.

Serpent started out as a simplified reactor physics code, but the capabilities of the current development version, Serpent 2, extend well beyond reactor modelling. It can be employed for traditional applications of reactor physics like spatial homogenization, but also for multi-physics simulations and neutrons-photons transport simulations. The latter application is the one of interest within the scope of this thesis.

Serpent is a Monte Carlo method based code because its main goal is to model complex geometries and interaction physics at the microscopic level with the best accuracy, even regardless of the computational cost. However, at the current stage, the use of Monte Carlo methods for nuclear reactor design is still not practical for computational requirements, even if there are some examples of Serpent application for the modelling of Small Modular Reactors (SMR) and Molten Salt Reactors (MSR) [8].

The first version of Serpent was developed in 2004 with the name of Probabilistic Scattering Game (PSG) aimed at lattice physics applications [8]. In this field, it was one of the most efficient codes among the other ones, mainly thanks to the use of a tracking routine based on the Woodcock delta-tracking method and the use of a single unionized energy grid for all the cross sections.

It is important to underline these two features of PSG, since they are still in use in the current version of Serpent. PSG (and later Serpent 1 and Serpent 2 too) used cross section libraries in ACE format (like ENDF/B-VIII.0 used in this thesis), as well as MCNP (Monte Carlo N-particle Transport Code).

Serpent 1 was written in 2007 with improvement in the geometry routine and in the interaction physics and was released by the OECD/NEA Data Bank in May 2009. The main limitations of this version were related to complex three-dimensional geometries for which the use of a single unionized energy grid for all the cross sections was a serious issue from the memory usage point of view and to the fact that parallelization in Serpent was still based on MPI (Message Passing Interface).

The code was rewritten starting from 2010 and now the available version is Serpent 2. The unionized energy grid approach is optimized and the parallel calculation based on both MPI and OMP (Open Multiprocessing) that allows to divide the calculation into multiple threads within the same computational unit, without increasing the overall memory demand.

Serpent 2 is a versatile tool that can be used to run neutron transport simulations in k-eigenvalue criticality source mode, typically useful for fission reactors, or in external source mode, useful for fusion systems like the ARC reactor analyzed in this thesis.

As well as many Monte Carlo particle transport codes, the basic routine geometry of Serpent is based on a constructive solid geometry (CSG) model. It consists of homogeneous material cells derived from elementary surfaces combined using boolean operators. However, there is also the possibility to implement CAD-based geometry types exploiting the stereolitography format, which is the approach used in this work (see chapter 3.3).

A fundamental aspect of any Monte Carlo code, related to the geometry, is the particle tracking for the simulation of the particle random walk. Serpent combines the more traditional ray-tracing based surface method with the rejection sampling based delta-tracking method (proposed for the first time by Woodcock in 1965 [9]). The latter method is the main one used by Serpent, improving the efficiency of the code in particular in geometries where the particle mean-free-path is long compared to the dimensions.

Its limitation is that it does not allow to use the track-length flux estimator but only the collision flux which has proven to be generally inferior [10] (it has low efficiency in small and optically thin detectors and in material with low collision density). For this reason Serpent 2 is implemented with some special techniques to overcome issues of this type [11].

Even if the delta-tracking method is known since the '60, it has not been employed in the common use Monte Carlo transport codes. Instead, Serpent 2 exploits the benefits that derive from this method. In particular, using the delta-tracking method, the random walk can be continuous even if there is a boundary between different materials so that it does not need to evaluate the distance between the particle and the nearest surface at each collision point as in the case of surface-tracking. Clearly this reduces the computational cost of the simulation. In this way the tracking is faster in complex geometries, like the geometry of ARC.

The delta-tracking method homogenizes the total cross section of the materials so that the sampled path length are valid over the whole geometry: in order to do this it is necessary to introduce the concept of virtual collision (a type of collision that does not affect the final result but that must be introduced in order to take into account that the whole domain has been homogenized). In general when the concept of virtual collision is introduced in a Monte Carlo code, it is necessary to "decide", from the probabilistic point of view, if a certain collision is a real collision or a virtual one. In Serpent 2 this is done with a rejection sampling method.

As stated before, the main limitation of the delta-tracking method is the impossibility to use the track-length flux estimator. For this reason Serpent 2 does not use only the delta-track method, but combines it with the surface-tracking method.

This is done passing to the surface-tracking method when the collision sampling efficiency is low. This is the case of materials with a cross section much smaller than the homogenized cross section obtained using the delta-tracking method, like in the presence of localized heavy absorbers or void regions [11].

Even if the track-length estimator has better performances than the collision estimator, its definition considers a response function constant over the sampled track, while in the case of the collision estimator the response function depends on the spatial coordinate by definition. In this way the collision estimator is superior than the track-length estimator in inhomogeneous region typical of coupled neutronics/thermal-hydraulics simulations [10].

The interaction physics data in Serpent are obtained from continuous-energy ACE format cross section libraries and the cross sections are reconstructed using a single unionized energy grid used for all reaction modes. In this way it is necessary to interpolate microscopic cross sections between tabulated values only once and it is possible to pre-calculate macroscopic cross sections, with the final result of dramatically reducing the computational cost.

The main drawback is that defining a single energy grid it is possible that some data will be redundant, producing a waste of memory that in some cases could be excessive to run the simulation.

This is a typical problem of large burnup calculation problems, so it is not the case of this work focused on the tritium breeding ratio and the power deposition of a fusion system.

Another interesting feature of Serpent 2 is the possibility to implement multi-physics coupling scheme. It is possible to couple Serpent 2 with CFD codes for the evaluation of the thermal hydraulics of the system.

Concerning the multi-physics applications, it is important to take into account also the photons which contributes, together with the neutrons, to the power deposition. Work in this field is still at an early stage and it will need testing in particular for what concerns the multi-physics interface. Serpent 2 allows to run coupled neutron-photon transport simulations since 2017 and this feature is used in the following calculations.

The output of Serpent 2 can be obtained defining detectors with user-defined flux tallies based on collision estimators for the calculation of reaction rates in the spatial domain. The output files are written in Matlab .m file format to ease the post-processing. There is also a geometry plotter to visualize the geometry of the model, for which is possible to choose different planes and different locations.

3.3 Geometry model

The first step in order to perform a Monte Carlo study using Serpent is to define the spatial domain. Serpent is mainly developed for the analysis of nuclear fission reactors and it allows to handle with simple and regular geometric shapes (like cylinders, prisms and spheres) or lattices (useful for the definition of fuel assemblies) and in order to do this it is embedded with predefined geometry cards exploiting a universe-based constructive solid geometry (CSG).

This is not the case of a nuclear fusion reactor, characterized by more complicated shapes. For this reason it is necessary to develop the geometry model with a dedicated CAD software. In this case, SolidWorks has been employed. The files produced with SolidWorks are then converted in STL format and imported in Serpent 2.

The stereolithography (STL) format is the simplest one used by CAD software like SolidWorks. It is based on the triangulation of curved surfaces, each one composed by a list of flat triangles defined by three points. In general the STL format is easy to read and handle, but it can be affected by numerical imprecision and it is not the best format for more complicated volumes. However, it has been demonstrated that this new geometry type work as expected, also in fusion application [12].

Using the stereolitography format it is not possible to use the standard routine used for CSG, but a new routine based on ray tests to determine if the point is inside or outside a solid. This method in general works well, but there are some complications in case of the presence of possible holes in the model and it is limited for what concerns the numerical precision (the latter issue can be fixed by the code itself).

In order to use a spatial domain in STL format in Serpent, it is required to define a box containing the domain and to create the background universe filled with void with the geometry cards provided by Serpent.

The design of the ARC reactor is still at a conceptual stage and the main goal is currently to optimize the plasma physics, to explore the behavior of REBCO tapes at very high magnetic fields and to maximize the TBR without compromising the other aspects of the reactor.

Therefore, at the state of the art, there are not very precise information about the dimensions of the reactor (for example about the length of the divertor leg, the height of the blanket tank and the dimensions of the coils), but [3] gives some useful values related to the main volumes for the neutronic analysis.

In the same article there is a simplified scale sketch (see fig. 2.2) of ARC, which has been used to obtain the main dimensions of ARC. Therefore, the final results is affected by some approximations since the CAD file of ARC was not available and, moreover, it is possible that the sketch is not completely precise.

Table 3.1 gives the comparison between the values obtained using SolidWorks and exploiting the few information found in the literature.

Table 3.1: Volumes of each material layer in the ARC reactor

	Volumes (SolidWorks) [m^3]	Volumes [3] [m^3]
Plasma	147	137
First wall	0.32	0.35
Inner VV	3.27	3.50
Cooling channel	6.58	7.04
Neutron multiplier	3.31	3.55
Outer VV	10.02	10.7
FLiBe blanket	304	241
PF coil shielding	43.5	49.2

The results are in good agreement, except for the FLiBe blanket. In any case this does not seem to be a problem, since it has been noticed that after around 70cm in the blanket the neutron flux reduces by more than two order of magnitudes, that can be considered acceptable if compared to the relative error of the Monte Carlo simulation [13]. Therefore, even if the volume obtained with SolidWorks is larger, we can expect that inside the extra volume there is a low amount of tritium produced and of deposited power.

The volumes of the components like the poloidal coils, toroidal coils and the central solenoid are not taken into account since they are not necessary in the scope of this thesis, while they can be useful for the evaluation of the neutron shielding and of the lifetime of the magnets. The eighteen support columns are not considered too because their influence on the neutronics is minimal due to their limited volume.

Some of the main dimensions used to define the spatial domain in Solidworks and obtain volumes similar to the ones described in the literature are shown in table 3.2.

Table 3.2: Main dimensions of the ARC reactor

	Length (SolidWorks) [cm]
Major radius	330
Minor radius	110
Height of the blanket tank	716
Radial dimension of the blanket tank	563
Height of the VV up to the divertor leg	405
Vertical distance between the centres of the divertors	617
Thickness of the inboard breeding blanket	70
Thickness of the ZrH_2 neutron shielding	25

In order to obtain the right dimensions and volumes, a fundamental aspect for the geometry model is the thickness of the layers between the vacuum chamber and the blanket tank, since they influence the neutron attenuation. Table 3.3 shows these values.

Table 3.3: Radial thickness of the double vacuum vessel [3]

	Thickness [cm]
First wall	0.1
Inner VV	1
Cooling channel	2
Neutron multiplier	1
Outer VV	3

For this neutronic study, the same radial assessment was considered for all the reactor, even if the divertors have a different structure in order to handle the higher heat fluxes. However, since the divertor is far from the neutron source, this aspect does not influence too much the neutron transport calculations [3].

After the definition of the dimensions and volumes of the different components, it is necessary to define the material for each of them. According to [1] and [3] the materials are:

- First wall $\longrightarrow$ Tungsten

- Inner VV $\longrightarrow$ Inconel 718
- Cooling channel $\longrightarrow$ FLiBe (Li_2BeF_4)
- Neutron multiplier $\longrightarrow$ Beryllium
- Outer VV $\longrightarrow$ Inconel 718
- FLiBe blanket $\longrightarrow$ FLiBe
- Blanket tank $\longrightarrow$ Inconel 718
- PF coil shielding $\longrightarrow$ Zircoium hydride (ZrH_2)

The compositions of Inconel 718 and FLiBe are shown in tables 3.4 and 3.5.

Table 3.4: Chemical composition of Inconel 718 (mass%) [14]

Element	Al	C	Co	Cr	Cu	Fe	Mo	Ti	Nb	Ni
%	0.52	0.021	0.11	19.06	0.02	18.15	3.04	0.93	5.08	53.0

Table 3.5: Chemical composition of FLiBe (mass%) [15]

Element	F	Li	Be
%	76.79	14.12	9.09

It is fundamental to consider the right composition, since each isotope is associated to a certain cross section, which influences the behavior of the neutrons inside the reactor. Also the smallest impurities must be taken into account, because it is possible that their consequences on the final results could be significant (this is particularly true in activation calculations).

Even if the coils are not required for the evaluation of the TBR and the power deposition in the blanket, their composition have been defined for completeness. In particular, it is important to remember that the central solenoid, the poloidal field coils and the toroidal coils work with superconductive magnets and for this reason they are put outisde the blanket. On the other hand, trim coils are mainly composed of copper, so they are located in the blanket near the plasma chamber.

The winding packs are composed of layers of different materials, but in this case they have been simulated as homogeneous isotropic materials with the composition shown in table 3.6 and table 3.7.

Another fundamental quantity to be defined for each material is the mass density. In fact the mass density influences the atomic density, so it is strictly related to the cross section of materials and, as a consequence, to the reaction rates. Mass density is function of the temperature, and the temperature profile evaluated in [1] using COMSOL is shown in fig. 3.1.

Table 3.6: Chemical composition of trim coils (mass%) [1]

	Copper	AISI 316 LN
%	53.9	46.1

Table 3.7: Chemical composition of central solenoid, poloidal coils and toroidal coils (mass%) [1]

	Copper	REBCO tapes (45% Cu, 55% Hastelloy)	AISI 316 LN
%	45.9	8	46.1

In order to define a material in Serpent it is necessary to select an average value of the mass density. This value has been obtained evaluating the arithmetic average of the temperature at the edge sides of each layer in which the temperature profile is almost linear (first wall, inner vacuum vessel, neutron multiplier and outer vacuum vessel) for the inlet distribution, then the same approach has been repeated for the outlet distribution.

Once an average value for the inlet and another one for the outlet has been computed for each layer, then the arithmetic average of these two values has been calculated. For what concerns the cooling channel the average outlet temperature has been considered $825\ \mathrm{K}$ and the inlet one SI800K, so the average temperature of the cooling channel is $812.5\ \mathrm{K}$.

According to other analysis, the inlet temperature in the blanket is $800\ \mathrm{K}$ and the outlet temperature $900\ \mathrm{K}$ [1].

Finally, some materials like Inconel 718 and FLiBe are used in different components, so in order to simplify the evaluation a single average temperature for each material has been considered, as shown in table 3.8.

The same table represents also the densities of each material that can be evaluated, knowing the temperature, with correlations found in the literature.

The mass density (and, as a consequence, the temperature) influences the cross section from a physical point of view since, for a given material, a higher mass density means a higher atomic density, so a higher probability of collision.

The effect of the temperature on the cross section is also related to the nuclear concept of Doppler broadening. The data library used in this work (ENDF/B-VIII.0) is available only for six temperatures between $300\ \mathrm{K}$ and $1800\ \mathrm{K}$ in $300\ \mathrm{K}$ intervals. In order to take into account the right temperature, in Serpent it is possible to initiate the Doppler broadening routine by adding the *tmp* entry followed by the temperature of the material in each material definition. It is important to consider both the physical and the nuclear phenomena.

Serpent enables to use thermal scattering cross sections to replace low-energy elastic scattering reactions for some moderator nuclides like hydrogen in water or

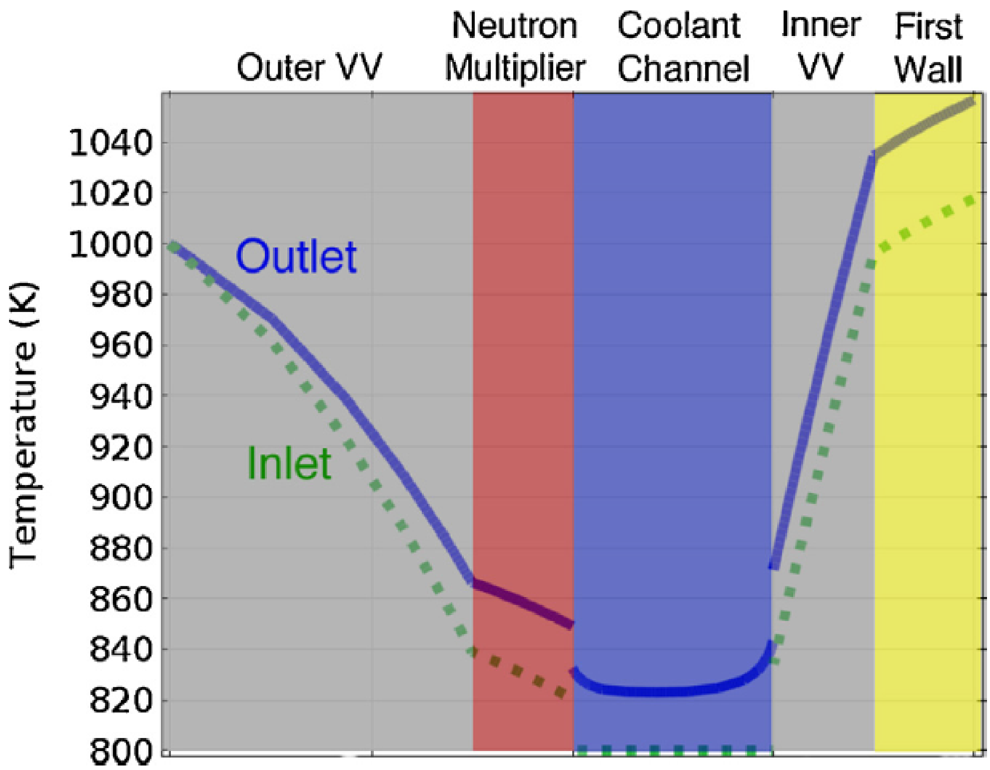

Figure 3.1: COMSOL model predicted temperature distribution across the vacuum vessel (with the plasma-facing surface on right) at both the channel inlet and outlet [1].

Table 3.8: Average temperatures and densities of each material inside ARC

	Tungsten	Inconel 718	FLiBe	Beryllium
T [K]	1029	930	830	844
ρ(T) [g/cm^3]	19.05 [16]	7.87 [17]	2.01 [18]	1.85

carbon in graphite or beryllium in FLiBe. This is particularly useful in thermal fission reactors: in such a system there will be significant errors in the spectrum and the results if the thermal scattering libraries are not used.

In the case of a fusion reactor like ARC the neutron spectrum is orders of magnitude faster (fig. 4.3 in chapter 4), so it is not necessary to use thermal scattering libraries.

The final spatial domain obtained with Solidworks is shown in fig. 3.2, where there is a poloidal section of the ARC with the definition of the main components of the reactor.

The layers of the vacuum vessel are not easily distinguishable because their thicknesses are on a much smaller scale. A detail of the vacuum vessel layers is shown in fig. 3.3.

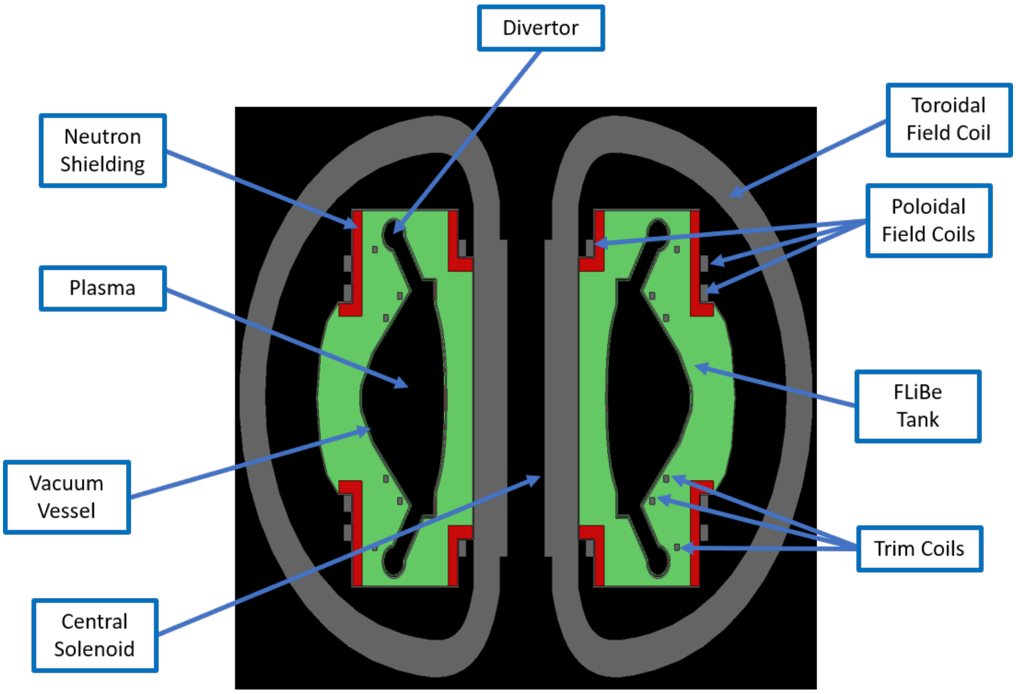

Figure 3.2: Poloidal section of ARC

Regarding the choice of materials, it is necessary to remember that the blanket in ARC must:

- convert the energy deposited by neutrons in heat for the power production;
- produce a certain amount of tritium so that the reactor is self-sufficient (which means a TBR larger than 1);
- shield the coils and cool the double vacuum vessel.

For these reasons the choice has fallen on FLiBe, an eutectic mixture of lithium fluoride (LiF) and beryllium fluoride (BeF_2), the most suitable liquid salt for the breeding of a sufficient amount of tritium [19].

There are already many studies about this particular molten salt since it has been proposed also in next generation fission reactors like the Fluoride Salt-Cooled High-Temperature Reactor (FHR) and the Molten Salt Reactor (MSR) [19].

Liquid FLiBe has been chosen also because its wide operating temperature window in liquid state, chemical inertness, similar thermal-hydraulics properties to water [1]. Moreover, the beryllium contained into the salt is useful for the neutron multiplication and it is also a good moderator improving the shielding.

FLiBe is isotopically enriched with 90% of ^{6}Li to maximize the tritium production: this is the main difference compared to FLiBe proposed for nuclear fission reactors where the FLiBe should be almost pure in ^{7}Li to avoid the production of tritium.

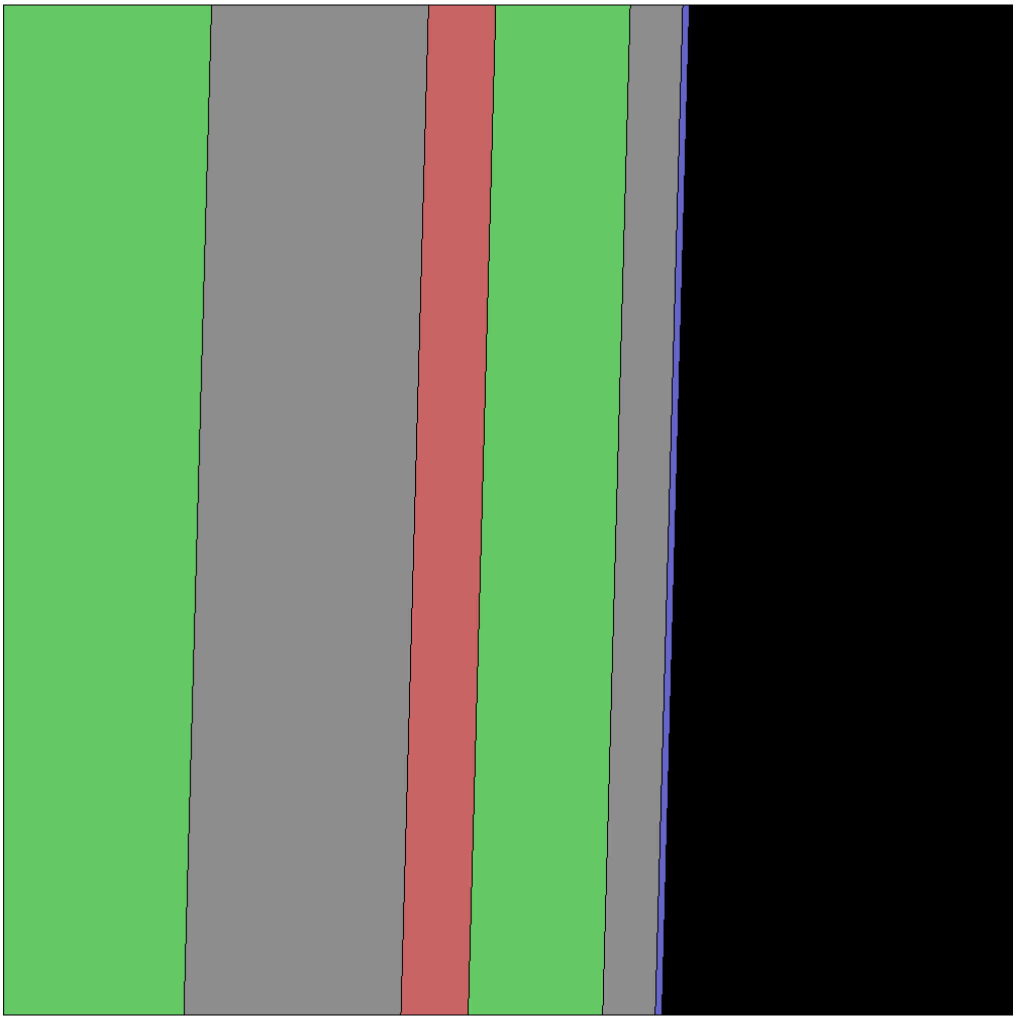

Figure 3.3: Radial build of the double wall vacuum vessel. From the right to the left: the plasma chamber (black), the first wall (blue), the inner vacuum vessel (grey) the first wall (blue), the cooling channel (green), the neutron multiplier (red), the outer vacuum vessel (grey) and the FLiBe blanket (green)

In fact ^{6}Li has a large tritium production cross section at low energies, while ^{7}Li is characterized by a threshold behavior, as shown in fig. 3.4. The reaction between a neutron and ^{6}Li is the following:

$$^6\mathrm{Li} + \mathrm{n} \rightarrow \mathrm{T} + ^4\mathrm{He} + \mathrm{n} + 4.8\,\mathrm{MeV}, \tag{3.12}$$

which is an exothermic reaction, generating substantial additional heating power. Also ^{7}Li is important since it is characterized by the following reaction:

$$^7\mathrm{Li} + \mathrm{n} \rightarrow \mathrm{T} + ^4\mathrm{He} + \mathrm{n} - 2.466\,\mathrm{MeV}, \tag{3.13}$$

which shows that the reaction is endothermic and that a neutron is consumed but

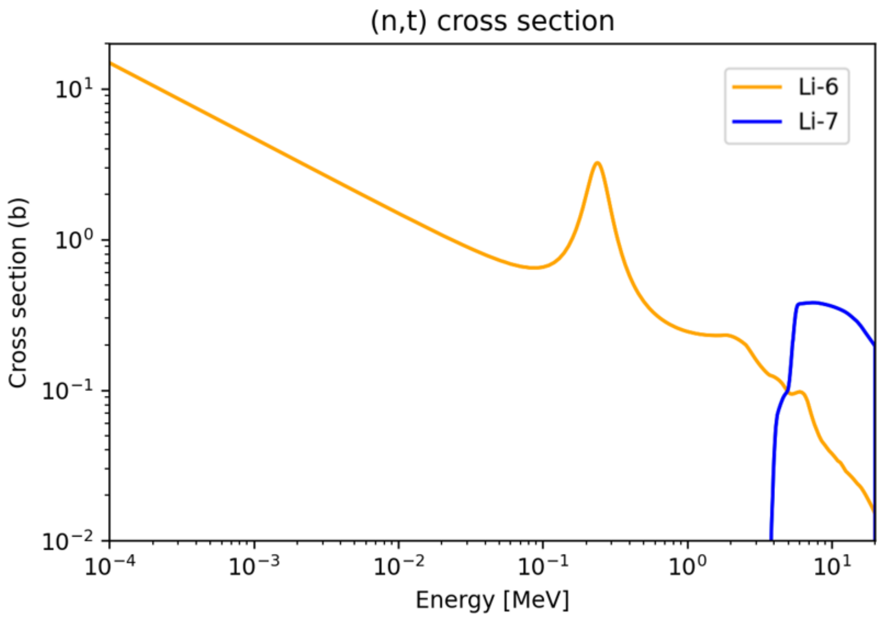

Figure 3.4: Tritium production cross section of ^{6}Li and ^{7}Li

another one is produced and this is fundamental to balance the neutron losses due to absorption or leakage.

Moreover it is necessary to have a value of TBR as high as possible. In fact a TBR equal to one is able to guarantee the self-sufficiency in an ideal system, but in a real system there are losses of tritium related to radioactive decay and nuclear reactions, so we need a TBR higher than one. On the contrary, if the TBR is too high there will be issues related to the tritium inventories.

Another positive aspect of FLiBe with respect to other liquid blankets like PbLi, is that it has a lower electrical resistivity reducing the MHD effects which are a not negligible aspect of hydraulics inside magnetic fields. This is of paramount importance in a system like ARC, which is featured by huge magnetic fields.

The material proposed for the first wall is tungsten, similarly to ITER, because it guarantees an optimal trade-off between the impurity radiation function and the sputtering yield, reducing the amount of impurities inside the plasma. In addition, tungsten is characterized by a high-energy neutron multiplication cross section (in the range of $7.5\,\mathrm{MeV}$ and $14.1\,\mathrm{MeV}$, see fig. 3.5) which contributes to the achievement of higher values of TBR.

The initial design proposed a thickness of $1\,\mathrm{cm}$, but then it was modified to $1\,\mathrm{mm}$ to avoid first wall temperature peaks and it is supported by a layer of structural Inconel 718 [13].

Inconel-718 was the initial choice for the double vacuum vessel. Inconel is a Ni-Cr based precipitation hardenable alloy, containing significant amount of Fe, Nb and Mo, with high corrosion resistance (because of the presence of nickel and chromium) at high temperature and there is good confidence that it will be able to survive any corrosive effects inside the FLiBe environment, also thanks to the low velocity of the liquid salt [1].

It has good thermo-mechanical properties and resilience in high temperature environment and this is the main reason for which it has been chosen as the main structural material. Inconel 718 used for ARC is extra-alloyed with Al, Ti, Nb, Co and Cu to increase mechanical and corrosion resistance [14].

However, the main drawback of Inconel is that it is a high activation alloy due to the content of nickel, molybdenum and niobium. This can be a problem for the maintenance and also for the disposal of Inconel at the end of its life.

The thickness of the inner and outer Inconel 718 vacuum vessels derives from structural integrity considerations, which were the main focus at first stages of the design together with the requirement of TBR>1.

In following steps of the design it will be interesting to study other materials like RAFM (Reduced-Activation Ferritic-Martensitic) steel Eurofer97 (the reference alloy of DEMO reactor) and V-15Cr-5Ti which are expected to guarantee a lower neutron activation, reminding that the main objective is still the structural integrity. Moreover the (n, 2n) and the capture cross sections of Eurofer97 and V-15Cr-5Ti at high energies are respectively higher and lower than the cross sections of Inconel 718, so the choice of this materials can have some implications also on the TBR because we expect that an higher number of neutrons can reach the blanket ([13]).

Beryllium is probably the best neutron multiplier in this case because it has a low energy threshold for (n, 2n) reactions (around $2\,\mathrm{MeV}$) and in this way it is possible to exploit the whole neutron flux spectrum. The (n, 2n) cross section of beryllium and tungsten are shown in fig. 3.5.

The beryllium layer is placed on the surface of the outer vacuum vessel, since it is not a structural material. The thickness is limited to $1\,\mathrm{cm}$ because of the cost and toxicity of beryllium. Moreover, if later design with different structural materials will allow to reach higher TBR, it would be a good choice to remove the potentially harmful beryllium layer. However, at the state of the art, it is still fundamental in order to obtain a TBR>1.

3.4 Source definition

Serpent was initially developed for k-eigenvalue criticality calculations, where the simulation is divided in cycles and the source distribution of each cycle is determined by the fission reaction distribution of the previous cycle. This is particularly useful in the case of critical or super-critical systems, like fission reactors for power production.

ARC is a fusion reactor, therefore can be defined as a non-multiplying system without any fission reactions, thus there is no reason to run a simulation for the evaluation of the k-eigenvalue in this case.

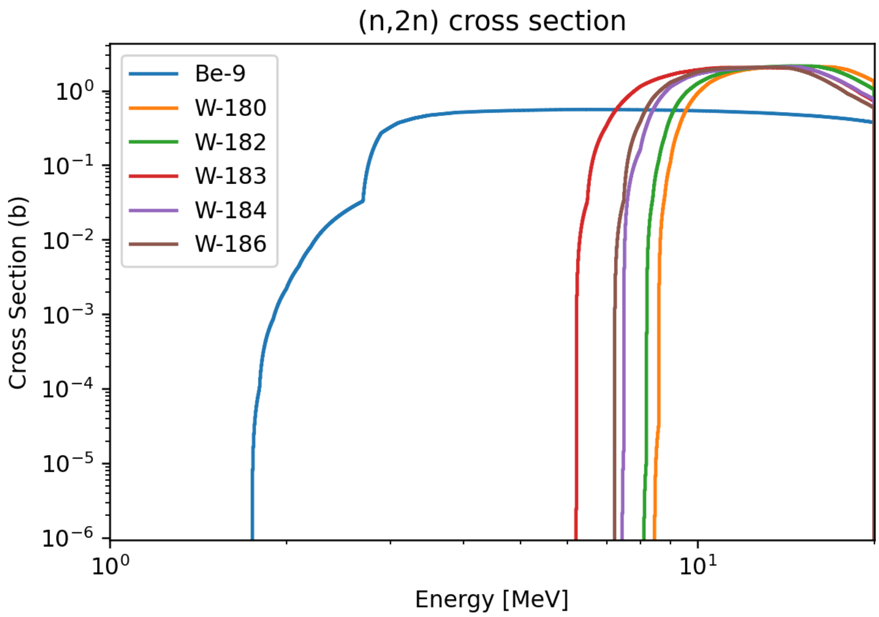

Figure 3.5: Neutron multiplication cross section of Be and W

From version 1.1.11 on, Serpent has made available an external source simulation mode which is not based on power iteration on the fission source, but on a user-defined source distribution. External source simulation mode is still very much under development, but there are already some articles where it has been used for the study of fusion devices. Some of them are listed on the official site of Serpent (e.g. [20], [21], [22] and [23]).

At first, a spatial distribution for the source must be defined, otherwise neutrons are started uniformly all over the geometry. Serpent offers the possibility to set a point source, a surface source, a source limited to only one material or to a particular cell and so on. In general the source calculation option do not allow to define source distribution as a function of the position, as occurs in the plasma of a fusion reactor.

For this reason, at first, a simplified spatially uniform source coinciding with the plasma chamber, except for the divertors and divertor legs, is defined. This is not a realistic source, but allows to obtain a first approximation of the neutronics in ARC and to understand if Serpent provides results that are consistent with the ones found in the literature. The results obtained with these source are shown in section 4.1.

However, an alternative strategy has been devised in order to overcome this issue. A series of concentric toroidal sub-domains is defined in order to simulate the magnetic surfaces inside the plasma and to assign to each sub-domain a weight equal to its volume-averaged neutron emission profile. In this way, a step-wise source distribution that approximate the actual source distribution is obtained.

This method has been preferred to the Serpent possibility to define a neutron source using a pre-generated source file from which Serpent will read the source points. The latter method is more precise, but it requires to define a huge file with information regarding the position of each source point in cartesian coordinates inside a toroidal geometry, the direction cosines of the emitted neutrons, the weight, the energy and the time at which the neutrons are emitted. Therefore, the creation of a pre-defined source distribution should be taken into account for future and more detailed works on ARC.

The choice of this simplified method is justified by the fact that, even with a spatially uniform source defined inside the plasma chamber, the results are similar to the ones presented in the literature. The non-uniform source was used to obtain the results in section 4.2.

Using the approach of the toroidal sub-domains, the selection of points where the neutrons are generated in Serpent is based on rejection sampling, and if the source material occupies a small volume of the geometry, the sampling efficiency can be increased by defining a bounding box around the region using the *sx*, *sy* and *sz* options of the *surf* card. Sometimes the efficiency is so low that the simulation cannot start. For this reason, a series of boxes that comprehend the different toroidal sub-domains is defined.

Concerning the energy distribution of the source, using Serpent it is possible to define energy distributions starting from nuclear reactions or defining discrete energy bins. However, in this study, the simplest option is used, which is the mono-energetic source. This is a reasonable choice since the neutrons produced by D-T fusion reactions have an average energy of $14.1\ \mathrm{MeV}$. Moreover, since there is no attenuation of the neutrons inside the plasma because there are not interactions, we can assume that the spectrum of the neutron source inside the plasma is monocromatic.

Another important information related to the energy of the neutrons is the source rate normalization. In fact, Serpent simulates at each cycle only one neutron as if the source rate was 1 neutron per second. Actually this is not true. In the ARC reactor (as any other fusion reactor) the source rate is much larger and it can be evaluated considering the energy associated to each neutron and the fusion power.

According to the design parameters proposed for ARC, the fusion power is $525\ \mathrm{MW}$. A good approximation derived from energy and momentum conservation is to consider that 80% of this power is carried by neutrons, resulting in a neutron power of $420\ \mathrm{MW}$ (the rest is carried by α particles).

Dividing this power ($420\ \mathrm{MW}$) with the energy associated to each neutron ($14.1\ \mathrm{MeV}$) the result is a source rate of $1.86 \times 10^{20}\ \mathrm{neutron/s}$. It is necessary to take into account this value in order to obtain consistent results for quantities like the neutron flux and the power deposition, which depend on the number of neutrons inside the system.

Instead, it is not required for the evaluation of the tritium breeding ratio, since it is defined as the "tritium produced in the blanket per each tritium burnt in the plasma" and, since for each tritium burnt there is a neutron produced, it can also be defined as "tritium produced in the blanket per each neutron produced in the plasma". This means that is correct to imagine a dummy source rate of 1 neutron/s to evaluate the TBR in a consistent way.

Unfortunately, Serpent lacks in the setting of the directional distribution. By default, all source neutrons are emitted isotropically and the only options allowed by Serpent is to define a mono-directional source or a file where each coordinate is associated to a different direction.

However, this problem is not a big issue in the case of a fusion reactor, since the neutron radiation inside the plasma can be considered almost isotropic. This is due to the fact that neutrons are neutral particles being not influenced by the magnetic field, so they have not a preferential direction (differently from the alpha particles which are charged and directed to the divertor target plates).

The assumption of a mono-energetic and isotropic volumetric source are not completely realistic, but they are a good first approximation.

In order to obtain a more realistic source, it is necessary to study the problem from the point of view of the plasma physics, which goes beyond the scope of this thesis.

3.4.1 Non-uniform source definition

The results shown in [1] provide some interesting information regarding the electron density and electron temperature profiles inside ARC's plasma that can be used to obtain a more realistic non-uniform source distribution for the simulation.

The explored regime is the I-mode, because it is proven to allow for easy control of density and impurities and is it characterized by a weak degradation of energy confinement time with heating power compared to standard H-mode.

Moreover it does not need Edge Localized Modes (ELMs) to regulates impurities during discharges and this is important since ELMs are not acceptable during the plasma operation since they are quite disruptive for plasma-facing components. As a consequence, the lifetime of the first wall and of the divertor with the I-mode regime is longer than the traditional H-mode.

Considering the experimental scalings from Alcator C-Mod I-mode profiles and assuming $\mathrm{T_e} = \mathrm{T_i}$, the temperature and density distributions, as a function of the ratio between the radial coordinate and the minor radius, shown in fig. 3.6, have been obtained.

From these plots it can be noticed that the volume-averaged electron temperature of ARC is $13.9\ \mathrm{keV}$ and the volume-averaged electron density $1.3 \times 10^{14}\ \mathrm{neutron/cm^3}$, while the maximum temperature is $27\ \mathrm{keV}$ and the maximum density $1.75 \times 10^{14}\ \mathrm{neutron/cm^3}$. Moreover, both the neutron both the temperature distributions are constant for values of r/a between 0 and 0.05.

At first, it is possible to obtain the density of the deuterium and of the tritium from the second plot considering that at a first approximation the two densities are equal (in order to maximize the fusion power) and each of the two densities is half

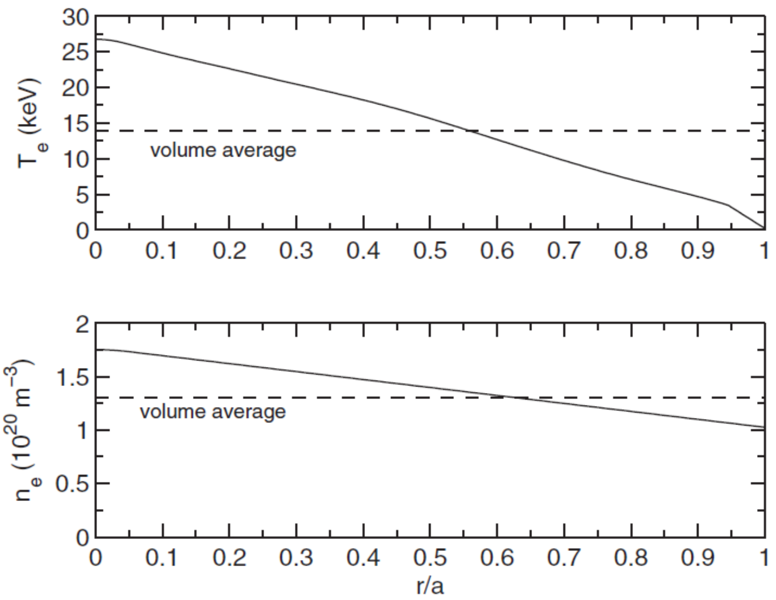

Figure 3.6: Radial profiles of electron temperature and electron density in ARC. [1]

the electron density (in order to preserve the quasi-neutrality inside the plasma). Therefore, the deuterium and tritium densities can be obtained simply dividing by two the the electron density profile.

From the temperature distribution it is possible to obtain the reaction coefficients $(\overline{\sigma v})$ in $\mathrm{reactions\,cm^3/s}$ as a function of the temperature, thanks to the following correlation [24]:

$$(\overline{\sigma v})_{DT} = 3.68 \cdot 10^{-12} T^{-2/3} exp(-19.94 \cdot T^{-1/3}) \tag{3.14}$$

with the temperature in keV.

The previous correlation is appropriate for low energy below or similar to $25\,\mathrm{keV}$ and, since the maximum temperature in ARC is $27\,\mathrm{keV}$, it can be used for the evaluation of the reaction coefficients in the plasma of ARC.

Once the distributions of the densities and of the reaction coefficients are known, it is possible to evaluate the reaction rate distribution in $\mathrm{reactions/cm^3/s}$ using the following expression:

$$RR = n_D n_T (\overline{\sigma v})_{DT}. \tag{3.15}$$

Reminding that each reaction produces only one neutron, this result coincides with the neutron emission profile in $\mathrm{reactions/cm^3/s}$.

The neutron emission profile is shown in fig. 3.7 and, as expected, it is orders of magnitude lower in the plasma edge compared to the values in the main plasma.

The equation of the neutron emission profile can be used to evaluate the volume-averaged neutron emission profile of each sub-domain with the following integral:

$$EP_{AVG} = \frac{1}{V} \iiint_V EP(r)\, d\vec{r} \tag{3.16}$$

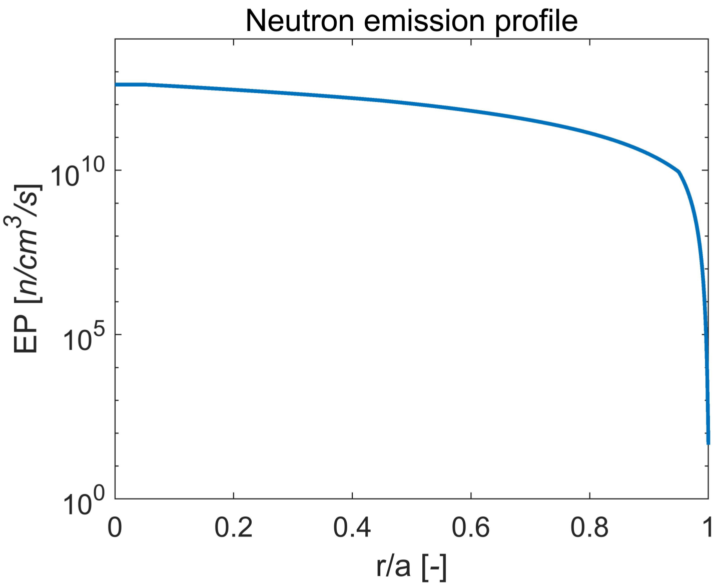

Figure 3.7: Radial profile of neutron emission density in ARC.

where $d\vec{r}$, for an axisymmetric torus, can be defined as:

$$d\vec{r} = 2\pi Rr\, dr\, d\theta \tag{3.17}$$

$$R = R_0 + r\cos\theta. \tag{3.18}$$

R_0 is the major radius, θ is the polar angle coordinate and r is the minor radius coordinate. Finally the integral to be solved is:

$$EP_{AVG} = \frac{1}{V}\iint_V EP(r)2\pi(R_0 + \cos\theta)r\, dr\, d\theta \tag{3.19}$$

and note that the term with $\cos\theta$ vanishes when integrating over θ.

The final result after all the simplifications is:

$$EP_{AVG} = \frac{4\pi^2 R_0}{V}\int_0^r EP(r)r\, dr. \tag{3.20}$$

The previous integral must be solved for each toroidal sub-domain in order to find the volume-averaged neutron emission profiles.

The average value is used as the weight assigned to each sub-domain. The solution of the integral (without dividing by the volume) is fundamental to preserve the total number of neutrons inside each sub-domain and to not distort the physics of the problem. The division by the volume is fundamental to normalize the results.

The number of sub-domains has been chosen as a trade-off between the accuracy of the result and the complexity of the evaluation due to the higher number of sub-domains. The final result is 9 sub-domains defined as shown in table 3.9 with the correspondent volume-averaged emission profiles.

Table 3.9: Definition of the toroidal sub-domains for the source distribution

	Radial position of the subdomain [cm]	EP_{AVG} [n/cm^3/s]
1^{st} subdomain	0 - 36	2.8794E+12
2^{nd} subdomain	36 - 44	2.0079E+12
3^{rd} subdomain	44 - 52	1.6463E+12
4^{th} subdomain	52 - 60	1.2401E+12
5^{th} subdomain	60 - 68	0.8714E+12
6^{th} subdomain	68 - 76	0.5711E+12
7^{th} subdomain	76 - 84	0.3381E+12
8^{th} subdomain	84 - 92	0.1704E+12
9^{th} subdomain	92 - 100	0.0646E+12

It is possible to perform all the previous evaluations considering some points of the plots in fig. 3.6 and from these points deduce the density and temperature distributions assuming that the profiles are piece-wise linear (this is consistent, for what concerns the density profile, with the typical feature of the I-mode of not having a particle transport barrier on the edge, while it is a simplifying assumption for what concerns the temperature).

All these results are obtained using simplified correlations and starting from the density and temperature profiles mainly because the knowledge about the I-mode is still limited if compared to the H-mode. For this reason it is not possible to derive directly global scaling law for predicting performances, but it is only possible to evaluate basic quantities like the temperature, the density and the pressure.

Finally, in the evaluation of the power deposition inside the blanket it will be important to consider also photons produced by interactions between neutrons and the different media. However, it is assumed that the source is composed exclusively by neutrons.

It is necessary to remark that the addition of the photons in the transport simulation introduces a new issue in a system like ARC. In fact Serpent is mainly developed for fission reactors, where the void regions represent a limited amount of the global volume, for example the thin region filled with helium between the fuel rod and the cladding.

Instead, in ARC, as in any other fusion reactor, we can say that the void is represented by the large volume represented by the plasma chamber: it is not really void but its density is almost zero. In ARC, the plasma chamber occupies around one third of the volume inside the blanket tank, so it is not negligible.

The main issue related to the presence of this large void region and of the photons is that, since the average cross section of the plasma is negligible compared to the majorant cross section computed by Serpent for the delta-tracking, there is the possibility that a photon enters in an infinite loop because of the high rejection probability in the low-density plasma.

In this case Serpent reports an error and stops the simulation, because by default the maximum number of photon loops in Serpent is 1000000 and then the simulation is terminated. In a fission reactor this event is very unlikely, since the void volume is negligible compared to the total volume.

In order to avoid this issue (that is not related to a geometry error but to the intrinsic nature of the problem) and to conclude the simulation without errors, it is possible to switch off the error completely using the *set inftrk* card.

3.5 Detectors

In order to obtain information about quantities like the neutron flux, the power deposition and the tritium breeding ratio using Serpent, we need to define a series of detectors inside the spatial domain.

Using Serpent it is possible to define detectors coincident with a cell, cartesian and cyindrical detectors and also lattice detectors, which are particularly useful for fission reactors.

Unfortunately, Serpent has not been developed for fusion reactor, so it is not easy to define detectors able to provide significant information about the spatial distribution of the quantities of interest. As well as the spatial definition, another key aspect for a detector in Serpent is the choice of the correct MT number, associated to a certain response function. In fact a detector in Serpent is able to estimate the following integral:

$$R = \frac{1}{V}\int_V \int_{E_i}^{E_{i+1}} f(\vec{r},E)\Phi(\vec{r},E)\, d\vec{r}\, dE \tag{3.21}$$

where R is the reaction rate and $f(\vec{r},E)$ is the response function. Therefore, the choice of the MT number influences the result of the reaction rate.

The value of the volume V is defined to be equal to one by default in Serpent and if we are interested in a reaction rate density, instead of a reaction rate, we need to divide by the volume of integration.

According to the quantities of interest, the following MT numbers have been chosen:

Response number	Reaction mode	Evaluated quantity
-55	Macroscopic triton production cross section	TBR
255	Microscopic triton production cross section	TBR of ^{6}Li and ^{7}Li
-80	Total energy deposition	Power deposition
0	None	Neutron flux

The MT number -80 is defined as the combination of responses for fission heating (in this case equal to zero), neutron heating based on KERMA (Kinetic Energy

Release in Materials) coefficients and analog photon heating. In this way it is possible to use a single detector to obtain information about the contribution of neutrons and photons on the power deposition.

In order to do this it is necessary to set in Serpent the neutron-photon coupled transport simulation on (using the *ngamma* card) and the energy deposition mode for energy deposition calculations (using the *edepmode* card).

Serpent is provided with four energy deposition modes: in this case, the mode 3 is the chosen one. It adds the photon power deposition estimation to the neutron heating rate evaluation with KERMA coefficients typical of the mode 2. The secondary photons are generated during the coupled neutron-photon transport calculation in reactions like inelastic scattering and radiative capture, atomic relaxation and bremsstrahlung and currently the model is able to take into account basic photon interactions like Rayleigh and Compton scattering, photoelectric effect and electron-positron pair production for photon energies ranging from $1\,\mathrm{keV}$ to $100\,\mathrm{MeV}$.

The energy deposition mode 3 is the most accurate spatially with minimal increase in the calculation time compared to modes 0 and 1 which are the simplest and less accurate ones [25].

For what concerns the volume for the normalization, we can set it to 1 for the evaluation of the TBR, since it is a reaction rate, while it must be set equal to the volume of integration in the case of the neutron flux (in order to obtain $[\mathrm{n/cm^2 s}]$) and of the power (in order to obtain $[\mathrm{MW/m^3}]$). This is quite easy if we are interested in global quantities, like the total TBR of the reactor or to the total volumetric power deposited in each component.

In the case of the TBR it is sufficient to define a detector that comprehend the whole volume and to the set the normalization volume equal to one and the normalization source rate equal to one too directly in the Serpent file.

In the case of the power deposition, we can define a series of detectors coincident with the different cells and to set the normalization volume equal to the cells volumes and the source rate equal to $1.86 \times 10^{20}\,\mathrm{neutrons/s}$. In this way we obtain a unique average value per detector, which can be an interesting result since it can be compared with the results found in the literature, but it is not as significant as a spatial distribution.

For example, the power distribution in different points of the volume is needed for the thermal-hydraulics evaluations of the blanket, in order to understand how and where dispose the power and which is the temperature profile inside the layers of the vacuum vessel.

In this respect it is fundamental to set the spatial domain of the detectors in a smart way. In fact we must avoid to define too many small detectors, because in this way we will obtain huge statistical error, and, on the other hand, too big detectors, because in this way we we will not find sufficiently refined results.

The strategy used in this work is to define a series of cylindrical detectors in order to cut the reactor in horizontal slices. The three coordinates of a cylindrical detector correspond in this case with the radial, the toroidal and vertical ones.

Since the ARC reactor can be considered toroidally symmetric, the detectors are defined with a single spatial bin for the integration in the toroidal direction. The vertical direction is important since we expect to have different results from the mid-plane to the top-plane, in this case it is used in order to define the position of the horizontally sliced detectors, but for each slice only one vertical bin is taken into account.

Finally, the radial direction is considered as the most significant one since we expect that the main variations occur radially. Therefore, the radial domain is set in order to include the regions of interest and the number of bins is defined in order to obtain significant results and at the same time to reduce the statistical error.

An implication of the use of a cylindrical detector is that the volumes of the bins change when the radius increases (differently from a cartesian detector where all the bins have the same dimensions), therefore we cannot normalize the volume directly with Serpent. This occurs because Serpent allows to set a single value for the volume of integration. For this reason it is necessary to compute the volumes of integration during the post-processing of the results.

However, the major complexity is related to the fact that Serpent is mainly developed for vertically straight geometries, like fission reactors where, in general, fuel rods and control rods are straight. With such a geometry it is easy to to define a detector (either cartesian or cylindrical) able to include the whole region of interest.

For example, if we want to obtain information related to a single fuel rod, we can define a cartesian detector and once the x and y coordinates are set it is sufficient to variate z in order to include all the fuel rod or only a limited part of it.

This is not possible with the geometry of the ARC reactor. In fact if we observe a poloidal section of ARC there are many curvilinear shapes: in this case, for a generic value of the radial coordinate, if the z direction varies, it will cut different materials, compromising the significance of the results.

This is the reason for which it seems a good idea to define cylindrical detectors thin in the z direction, so that for each radial coordinate there is only one material. However, it is fundamental to underline again that the detectors can't be too thin, otherwise the statistical error will be huge.

The first set of cylindrical detectors is used for the evaluation of the neutron flux inside the reactor:

- a detector in the equatorial region with a thickness of $20\ \mathrm{cm}$ and with the base coincident with the mid-plane of the reactor;
- a detector with the center at the height of $195\ \mathrm{cm}$ and a thickness of $10\ \mathrm{cm}$;
- a detector in the polar region between $341\ \mathrm{cm}$ and $360\ \mathrm{cm}$ in order to include only the FLiBe blanket veritcally.

It is useful to define more than one detector so that it can be noticed how the flux varies radially but also at different heights.

Finally, there is also a detector that comprehends all the reactor divided in radial bins, in order to obtain a more direct result, even if less refined.

Another important set of cylindrical detectors is defined for the evaluation of the power deposition. In this case the information is useful in order to understand how to extract the energy deposited by neutrons and photons in the vacuum vessel and in the blanket. Obviously, the power deposited is a direct consequence of the neutron flux and of the material, so the two results are strictly connected.

Also in this case there is an equatorial detector, one put at the base of the upper divertor leg and the third in the poloidal region. Moreover, for what concerns the equatorial and the 'half height' detectors, other two smaller detectors are defined to give a more precise information about the inboard and outboard sides of the vacuum vessel.

This is particularly useful because inside the vacuum vessel there is the channel of FLiBe, which carries out a fundamental role for the cooling of the vacuum vessel. Moreover, it is required to know the power deposited in the two layers of Inconel 718 of the vacuum vessel to be sure that the thermo-mechanical limits are not exceeded.

Tables 3.10 and 3.11 summarise the positions and dimensions of the different detectors with the respective number of bins.

Table 3.10: Detectors for the neutron flux evaluation

	Radial range [cm]	bins [-]	Toroidal range [°]	bins [-]	Vertical range [cm]	bins [-]
Det1	140-565	425	0-360	1	0-20	1
Det2	140-565	425	0-360	1	190-200	1
Det3	140-565	425	0-360	1	341-360	1

Table 3.11: Detectors for the power deposition evaluation

	Radial range [cm]	bins [-]	Toroidal range [°]	bins [-]	Vertical range [cm]	bins [-]
Det1	140-565	425	0-360	1	0-20	1
Det2	210-221	110	0-360	1	0-20	1
Det3	437-450	130	0-360	1	0-20	1
Det4	140-565	425	0-360	1	190-200	1
Det5	238-249	110	0-360	1	190-200	1
Det6	314-327	130	0-360	1	190-200	1
Det7	140-505	365	0-360	1	341-360	1

Finally, regarding the TBR, in general it is sufficient one detector that comprehend the whole reactor for the evaluation of the tritium production in the system. In fact the TBR is, by definition, a global quantity, so a single value can be sufficient to understand if the reactor can be self sufficient or not.

However, it can be interesting to define additional detectors inside the reactor in order to obtain information about the regions where the major quantity of tritium is produced and which is the contribution of ^{6}Li and ^{7}Li in the production of tritium. Therefore, another set of cylindrical detectors is defined for the evaluation of TBR, as shown in table 3.12.

Table 3.12: Detectors for the tritium production rate

	Radial range [cm]	bins [-]	Toroidal range [°]	bins [-]	Vertical range [cm]	bins [-]
DetTBR1	140-565	425	0-360	1	0-10	1
DetLi6	140-565	425	0-360	1	0-10	1
DetLi7	140-565	425	0-360	1	0-10	1
DetTBR2	140-565	425	0-360	1	190-200	1
DetTBR3	140-505	365	0-360	1	341-360	1

It is fundamental to remember that for the evaluation of the Tritium production associated to ^{6}Li and ^{7}Li (DetLi6 and DetLi7 in table 3.12) it is necessary to use a positive MT number, since we are interested not to a material total reaction rate, but to an isotopical one. Therefore, the result obtained with Serpent in this case is associated to a microscopic cross section, which means that during the post-processing the results have to be multiplied by the atomic densities of ^{6}Li and ^{7}Li in order to obtain consistent results.

Chapter 4

Results

In this chapter the results of the simulations with the different source definitions performed with Serpent are presented and compared.

Section 4.1 shows the results with the spatially uniform source and section 4.2 the ones obtained with the non-uniform source.

All the results are evaluated using the nuclear reaction data library ENDF/B-VIII.0, which is the latest release among the ENDF/B nuclear libraries.

A first simulation was carried out considering the toroidal coils and the central solenoid too, but the difference between the results of this simulation compared to the ones of the simplified spatial domain does not justify the use of a more complex domain. In particular the differences related to the TBR and the power deposition are negligible, also taking into account the relative error.

The results with the non-simplified domain were obtained with 10^7 neutrons divided in 100 batch, in order to perform a faster simulation, and are shown in tables 4.1 and 4.2, and can be compared with the results of the non-uniform source in tables 4.8 and 4.9.

Table 4.1: Global values of TBR

Total	Cooling channel	Blanket
1.0863±0.0005	0.2528±0.0002	0.8310±0.0005

The use of a simplified spatial domain allows to obtain a lower statistical error reducing the computational time too. This solution is particularly useful considering that the neutron-photon simulation with Serpent is quite expensive from the point of view of the computational cost. Obviously, this simplification can not be performed if the aim of the simulation is to evaluate the shielding of the coils.

Table 4.2: Average volumetric power deposition in each material layer in the ARC reactor

	Voluetric power $[\mathrm{MW/m^3}]$
First wall	23.15±0.03
Inner VV	10.90±0.01
Cooling channel	12.03±0.01
Neutron multiplier	6.527±0.005
Outer VV	7.321±0.004
FLiBe blanket	0.8392±0.0003
PF coil shielding	0.00273±0.00006

4.1 Spatially uniform source

The quantities of interest estimated with the spatially uniform neutrons source are the neutron flux and the neutron spectrum (subsection 4.1.1), the tritium breeding ratio (subsection 4.1.2) and the neutrons and photons power deposition (subsection 4.1.3).

The input files used for the Serpent simulations with the spatially uniform source can be found at [26].

4.1.1 Neutron flux

The results shown in this chapter were obtained considering 10^8 neutrons divided in 100 batches using the external source mode of Serpent. They are referred to a simplified spatial domain that comprehends the plasma chamber, the vacuum vessel, the blanket tank but not the toroidal field coils and the central solenoid.

Actually, even with 10^8 neutrons, in the external regions of the reactor, the neutron flux (which influences all the other quantities of interest) is associated to high relative errors because they are far from the neutron source. However, even inside the statistical error, the flux is orders of magnitude lower than the maximum one at the center of the reactor, so it is not of interest for the purpose of this thesis, focused on the neutronics of the blanket. Therefore, the important thing is to guarantee a low statistical error inside the FLiBe blanket itself.

The first set of simulations was carried out considering a spatially uniform source of neutrons inside the plasma chamber. This is a simplified assumption, but it is useful in order to have a first insight into the problem. A source definition of this type means that the probability of a neutron being generated in a point instead of another is the same, so it does not take into account that the neutron generation is higher in the central part of the plasma compared to the plasma edge.

In this case the domain where the neutron source is defined coincides with the whole plasma chamber, except for the divertor legs and the divertors, because we can expect that in these regions the density and the temperature are so low that the neutron production is negligible.

The neutron flux is the most important quantity that can be evaluated, since all the reaction rates and reaction rate densities depend on the neutron flux, according to equation (3.21).

By default Serpent sets to one the volume of integration. In order to obtain the neutron flux in units of $\mathrm{neutrons/s/m^2}$ it is fundamental to divide the result obtained with Serpent by the volumes of the spatial bins of the detector during the post processing.

The neutron flux has been evaluated at first on the whole blanket as shown in fig. 4.1. As expected, the highest values of the neutron flux correspond with the

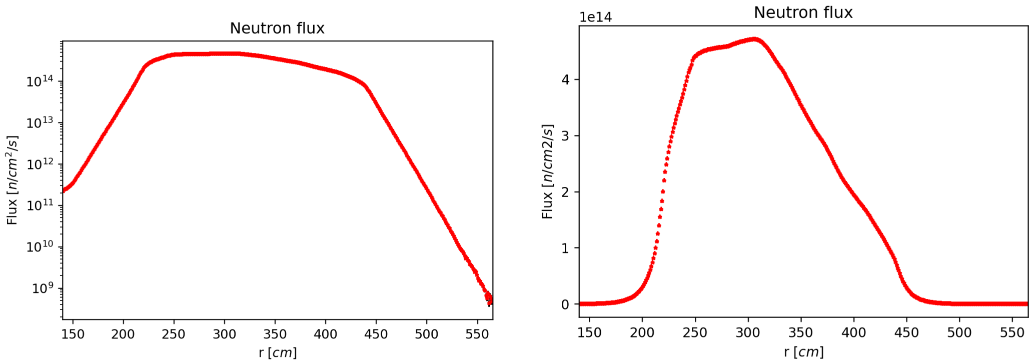

(a) *Radial neutron flux (logarithmic scale)* **(b)** *Radial neutron flux (linear scale)*

Figure 4.1: Radial neutron flux in the whole breeding blanket tank in logarithmic (a) and linear (b) scale. The error bars are not visible because the relative error is too low.

central region occupied by the plasma, then the neutron flux decays exponentially in the blanket.

In particular, the blanket is able to strongly reduce the neutron flux shielding the external coils composed of superconductors. In fact, after the region occupied by the blanket tank (between $140\,\mathrm{cm}$ and 565cm) the flux is three orders of magnitude lower than the maximum neutron flux, thanks to the shielding effect of FLiBe inside the blanket.

After this first evaluation it is useful to consider the neutron flux in smaller volumes at different heights, in particular in the equatorial region, at the base of the upper divertor leg and above the divertor in the polar region (fig. 4.2). The dashed lines in the plot represent the vacuum vessel layer subdivision.

In fig. (a) and fig. (b) there is a flat part in correspondence with the plasma. The neutron flux in the flat part is in the order of $10 \times 10^{15}\,\mathrm{neutrons/cm^2/s}$, higher than the maximum value of figure 4.1. This is due to the fact that in fig. 4.1 the detector comprehends all the height of the blanket and not only the plasma (as in the case of fig. 4.2 (a) and (b)), so the average result is lower. In fact, the neutron flux in the blanket above the divertor (and also below, because of the symmetry of the reactor) is smaller.

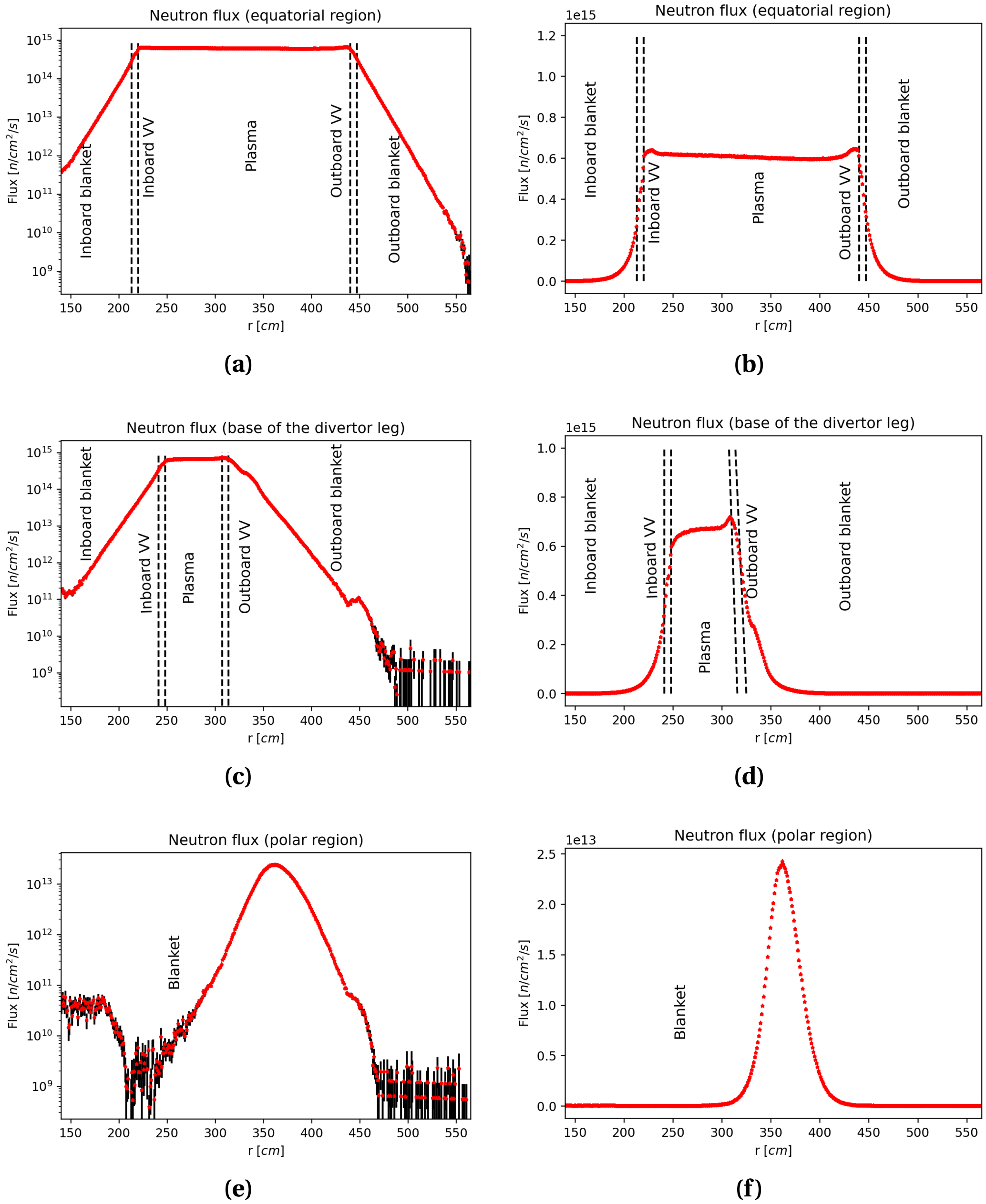

Figure 4.2: Neutron flux in the equatorial region (a) (b), at the base of the upper divertor leg (c) (d) and above the upper divertor (e) (f), in logarithmic (left column) and linear (right column) scale. The error bars are visible in the logarithmic plots.

The plots in fig. 4.2 have a higher statistical error than fig. 4.1, either because they are the result of smaller detectors and because they are located far from the neutron source (plot (c)), so it is more difficult to obtain statistical information because it is less probable that the random walk of neutrons passes through the domain of these detectors.

The error bars related to the statistical error farther form the neutron source are visible in particular in fig. (a), (c) and (e) where the the scale is logarithmic. However, in fig. (b), (d) and (f), where the scale is linear, it is clear how the influence of these errors is negligible compared to the values of neutron flux in the central part of the reactor.

From a physical point of view, we expect that the flux decays exponentially inside the blanket because the FLiBe is not a multiplying material, so the results in fig. (b), (d) and (f) are consistent with the physics of the problem, even if the statistical error is high. For this reason the choice of increasing the neutron population to have low statistical errors far from the plasma chamber is not motivated, since we are not interested in precise results in the extreme regions of the blanket.

On the other hand, the error bars in the region near to the plasma, where there are many neutrons and the statistical information is more detailed, are not visible because the statistical error is low.

It is also possible to observe a not so realistic result due to the use of a hypothetically spatially uniform source: the values of the neutron flux at the equatorial region and at the base of the divertor upper leg are similar, because the generation probability of a neutron is the same in the whole source spatial domain.

The same strategy of positioning of the detectors will be used also for the other quantities of interest (TBR and power deposition).

Another quantity related to the neutron flux is the neutron flux spectrum. In fact it is not only important to have information about the number of neutrons in general, but also to know how many neutron have low or high energies. This is due to the fact that the cross sections and the response of materials after the interaction with neutrons depend on the energy of the neutrons. For example it is possible to evaluate the neutron flux spectrum inside the plasma chamber, the neutron multiplier the FLiBe blanket and the blanket tank as shown in fig. 4.3 (a).

In order to evaluate the neutron spectrum it is necessary to define an energy grid.

In this case the energy interval considered is included between $0.1\,\mathrm{keV}$ and $20\,\mathrm{MeV}$, since the neutrons are produced by the D-T reactions with an energy of $14.1\,\mathrm{MeV}$ and we do not expect to have faster neutrons. Moreover, because the neutrons of a fusion reactor are generally faster than neutrons of a fission reactor, it does not make sense to go under too low energies. The energy range has been divided in equal lethargy-width bins, in order to obtain a regular subdivision of the energy.

As expected, the peaks are in correspondence of $14.1\,\mathrm{MeV}$, the energy of the source neutrons. Another characteristic that appears from the plot is that the values of the spectrum inside the beryllium neutron multiplier are higher than the one in the plasma chamber and this is consistent with the neutron multiplying property of beryllium. In particular, this result underlines the importance of the beryllium layer for the production of tritium, because without it probably there would be too few neutrons to have TBR>1.

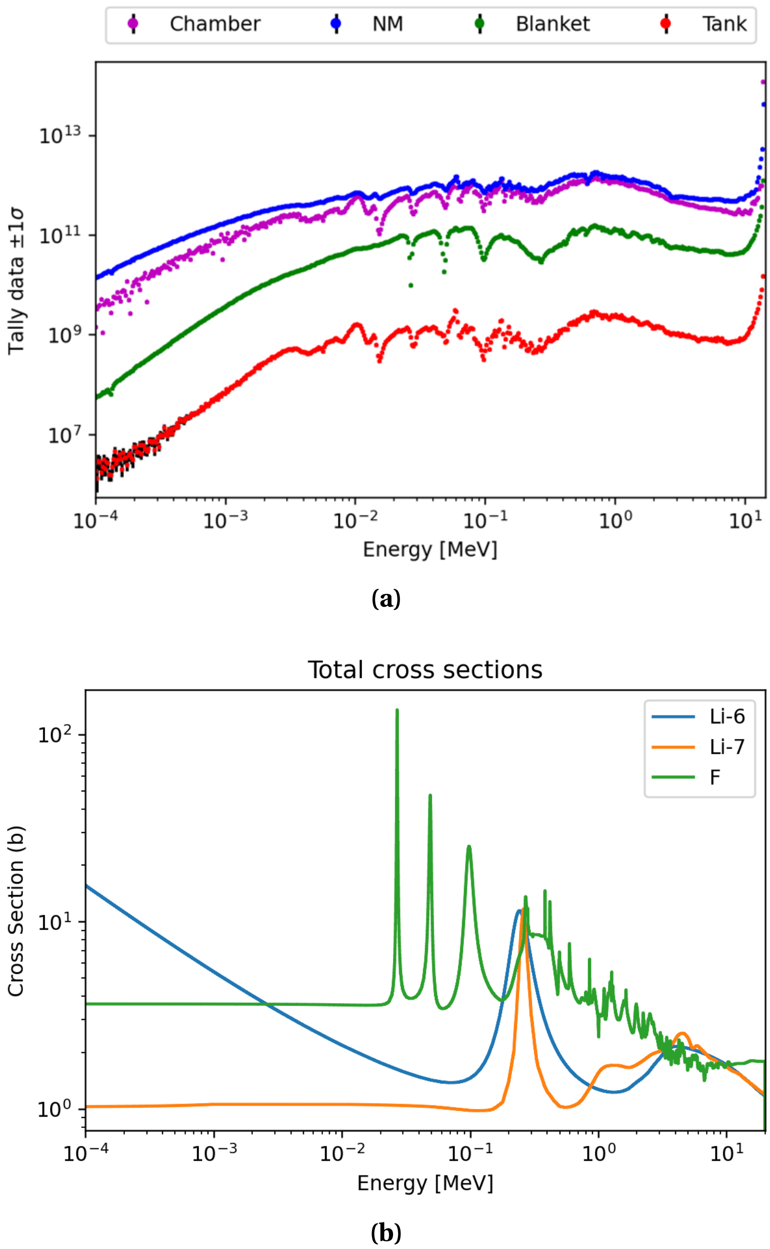

Figure 4.3: Neutron flux spectrum (a) in the plasma chamber, neutron multiplier (NM), breeding blanket and breeding blanket tank. The error bars are visible only for the breeding blanket tank because for the other components the statistical error is too low. Figure (b) shows the total cross sections of fluorine, ^{6}Li and ^{7}Li

Concerning the spectrum of the FLiBe blanket, there are some sort of peaks between 10^{-2} MeV and 10^{-1} MeV, explainable by the fact that the cross section of fluorine has some resonance peaks in this energy interval. Moreover, in FLiBe the spectrum seems to decrease faster at lower energies, mainly because ^{6}Li has an high cross section at lower energies. The drop between 0.1 MeV and 1 MeV in the blanket neutron spectrum is due to the presence of a peak in the cross section of ^{6}Li and ^{7}Li in this range.

These characteristic features of the cross sections of fluorine and lithium are shown in fig. 4.3 (b), which allows to compare the results of the neutron spectrum with the nuclear data of these isotopes.

Finally, the spectrum in the blanket tank is several orders of magnitude lower, underlying the moderating effect of the FLiBe blanket. Not only the neutron spectrum is lowered in general, but it is also softened thanks to the FLiBe. The reduction of the fast flux reduces the damage neutron rates in terms of displacement per atoms (DPA) and of helium production in the blanket tank. Lower values of DPA mean reduced degradation in thermal performances, which is another improvement guaranteed by the presence of the FLiBe blanket.

In this way the blanket tank and the external coils are strongly protected by the neutrons. The shielding of the coils is obtained also thanks to the presence of 25 cm thick shielding plates of zirconium hydride at poloidal field coils location. The only coils which are not shielded are the trim coils, located inside the blanket and not made of superconductive materials but of copper.

4.1.2 Tritium breeding ratio

The first result obtained is the global TBR, evaluated with a detector that includes the whole reactor. The TBR is equal to 1.0845±0.0001 (table 4.3), which is slightly lower than the result of the initial design (TBR = 1.1±0.0001 [1]), because of the addition of the two long divertor legs and the consequent reduction of the FLiBe volume, but it is comparable with the result obtained in [3] of 1.08±0.004.

In this design the TBR is higher than 1 primarily thanks to the limited amount of structural materials, which usually does not contribute to breeding, and to the presence of the non-structural neutron multiplier layer of beryllium.

Table 4.3: Global values of TBR

Total	Cooling channel	Blanket
1.0845±0.0001	0.2717±0.0001	0.8104±0.0001

This result can be considered a partial verification of the model consistency in spite of the approximations introduced in the source definition and in the reactor geometrical model.

In further detail, it is possible to evaluate the radial distribution of the reaction rate of neutrons with lithium inside ARC at the mid-plane (detector DetTBR1 in table 3.12, chapter 3.5). The result is shown in fig. 4.4.

As expected, the reaction rate vanishes in the central region occupied by the

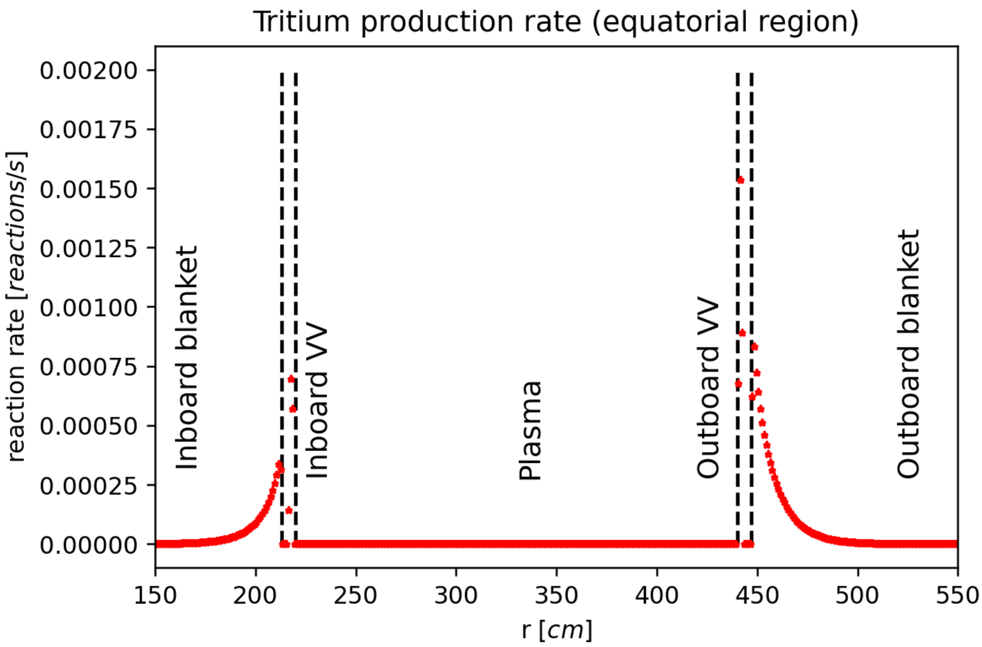

Figure 4.4: Radial distribution of the reaction rate in the equatorial region. The error bars are not visible because the scale is linear and, even if the relative error is high for the lowest and highest values of the radial coordinate, their influence on the final result is negligible because in these regions the reaction rate is low compared to the values near the plasma.

plasma between $220\,\mathrm{cm}$ and $440\,\mathrm{cm}$ from the center of the reactor. Another interesting feature is the peak coincident with the cooling channel inside the vacuum vessel.

This result can be explained by the fact that many neutrons reach to the cooling channel before being absorbed, since it is near to the plasma (there is only the 1 cm inner vacuum vessel between the neutron source and the cooling channel).

Another possible explanation is that between the plasma and the cooling channel, due to the limited thickness between the two regions, there is a low probability of having a big number of scattering events. In this way the neutrons that arrive to the cooling channel are still characterized by a fast spectrum, increasing the number of tritium production collisions with ^{7}Li. This has not only a direct consequence on the TBR, but contributes also to the generation of new neutrons thanks to the reaction neutron-^{7}Li, indirectly affecting the increase of TBR.

These speculations are confirmed by the comparison between the plots in fig. 4.5. These two plots represent the radial distribution of the reaction rate too, but referred to ^{7}Li and ^{6}Li. At first, it can be noticed how the ^{6}Li contributes more to the TBR with respect to ^{7}Li in absolute value by three orders of magnitude, either because the lithium used in FLiBe is enriched with 90% of ^{6}Li and because ^{7}Li can produce tritium only if the neutron has an energy higher than $2.466\,\mathrm{MeV}$.

However, the relative importance of ^{7}Li in the channel is higher than ^{6}Li, because

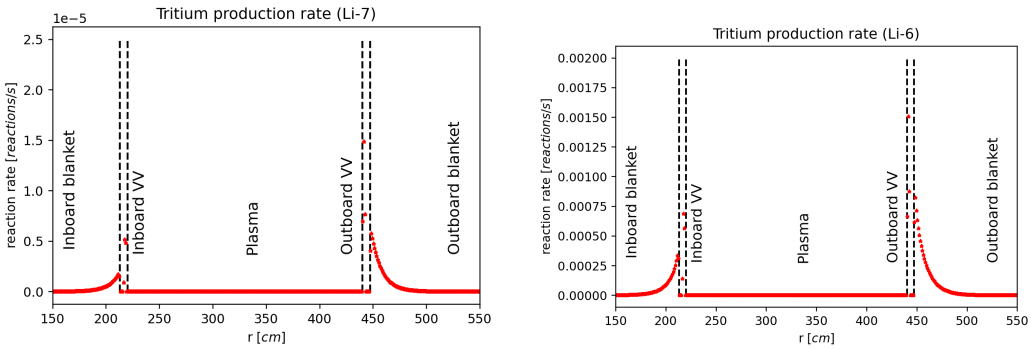

(a) *Radial reaction rate relative to ^{7}Li* **(b)** *Radial reaction rate relative to ^{6}Li*

Figure 4.5: Radial distribution of the reaction rate relative to ^{7}Li (a) and to ^{6}Li (b) in the equatorial region. The error bars are not visible because the scale is linear and, even if the relative error is high for the lowest and highest values of the radial coordinate, their influence on the final result is negligible because in these regions the reaction rate is low compared to the values near the plasma.

the neutrons in the channel are faster than the neutron that arrive in the blanket.

Even if the direct contribution of ^{7}Li to the TBR is negligible, it is still important because each neutron-^{7}Li interaction that produces a triton, produces another neutron too. This slower neutron has even a higher probability of interaction with an atom of ^{6}Li for the production of another triton (see fig. 3.4), for example.

After the first peak (both on the inboard and outboard side), the reaction rate decreases exponentially and this is consistent with the exponential decay behavior of the neutron flux inside a non-multiplying medium.

Additional information can be obtained defining other detectors at different heights, like DetTBR2 and DetTBR3 described in table 3.12 (chapter 3.5). The detector DetTBR2 is located at the base of the upper divertor leg and detector DetTBR3 in the blanket above the upper divertor.

The results are shown in fig. 4.6 and fig. 4.7 respectively. In fig. 4.6, on the outboard side, there is a drop around $330\,\mathrm{cm}$ due to the presence of a trim coil where no tritium is produced.

The peak on the right is not as localized as the one on the left, because the vacuum vessel on the right is very sloped so the detector intersect different material in the vertical direction. In this way it is not possible to identify the different materials (in fact in the plot there are not any points where the reaction rate is null inside the vacuum vessel).

The solution to prevent this problem would be to define an extremely thin detector, but this will cause the increase of the statistical error.

The reaction rate of neutrons with lithium for the production of tritium in the blanket above the upper divertor, as shown in fig. 4.7, has a central peak coincident with the radial position of the divertor. This is a reasonable result since there are many neutrons arriving from the divertor, while for different values of the radial

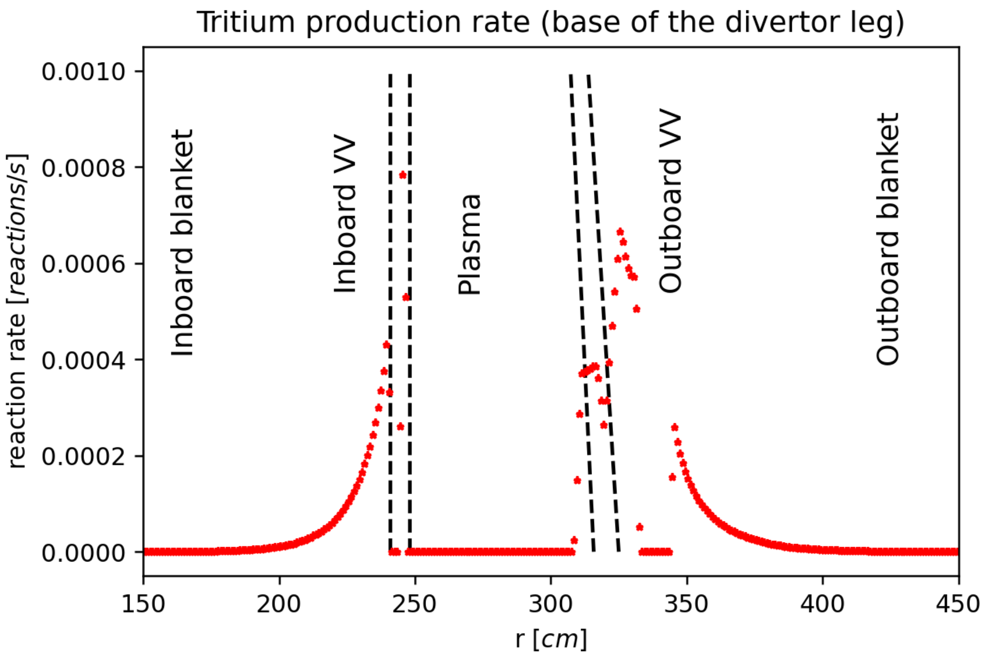

Figure 4.6: Radial distribution of the reaction rate at the base of the upper divertor leg. The error bars are not visible because the scale is linear and, even if the relative error is high for the lowest and highest values of the radial coordinate, their influence on the final result is negligible because in these regions the reaction rate is low compared to the values near the plasma.

coordinate the neutrons have to travel inside the blanket before producing tritium in the detector, so there is an exponential decay.

Another feature observable in the plot is that the values of the reaction rate above the divertor are three orders of magnitude smaller than the equatorial one, underlying the importance of the cooling channel for the production of tritium.

Moreover, comparing the total TBR relative to the channel with the total TBR in the blanket, the results are 0.2717 and 0.8104 respectively. This means that around 25% of the TBR is provided by the channel, even if its volume is only 1% of the total against the 50% of the blanket.

According to to these results, a possible improvement for ARC could be the increase of thickness of the cooling channel, further increasing its relative contribution to the TBR. Another possible benefit of a thicker cooling channel is that the outer vacuum vessel is reached by a lower number of neutrons.

This is important in order to preserve the mechanical properties of the outer structural layer, which is the most important one for the structural integrity of the vacuum vessel (in fact its thickness is $3\,\mathrm{cm}$ versus $1\,\mathrm{cm}$ of the inner structural layer) [13].

The sum of the TBR inside the cooling channel and inside the blanket is not

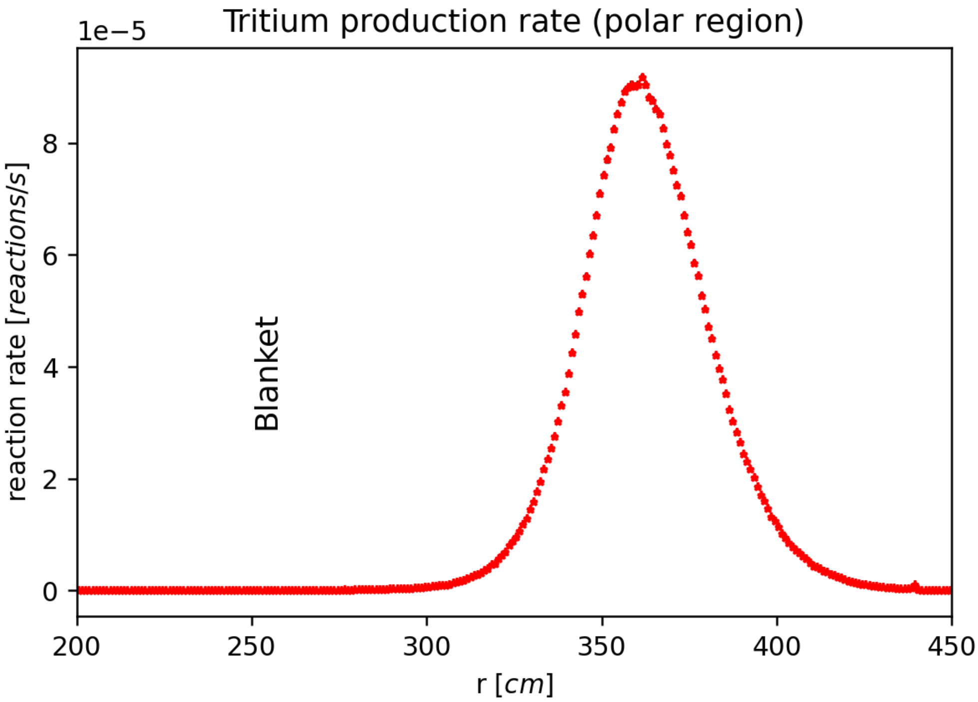

Figure 4.7: Radial distribution of the reaction rate in the blanket above the upper divertor. The error bars are not visible because the scale is linear and, even if the relative error is high for the lowest and highest values of the radial coordinate, their influence on the final result is negligible because in these regions the reaction rate is low compared to the values near the plasma.

exactly equal to the global result because the three values of the TBR are evaluated with different detectors, each one independent to the other and with different statistics.

4.1.3 Volumetric power deposition

Another important quantity to be evaluated is the volumetric power deposition. In fact it is important that at each instant the cooling channel is able to remove the power deposited in the structural vacuum vessel, avoiding damages to the vacuum vessel itself. Moreover, the power deposited in the FLiBe blanket must be extracted for the production of electrical power, so it is of paramount importance to know where the energy of neutrons and photons is mainly deposited.

This result can be used also as fundamental input for the thermal-hydraulics analysis of the FLiBe flow inside the blanket of ARC.

Initially, the simulations for the estimation of the power deposited inside the blanket of ARC were performed using MT=-4, described as "macroscopic total heating cross section" on the Serpent manual. This definition is not so clear, since it does not define the meaning of heating cross section.

Moreover, the results obtained in this way were clearly different from the results shown in the literature in some cases. For example, the volumetric power deposition inside the inner vacuum vessel was estimated to be $16.776\,\mathrm{MW/m^3}$ against the result of $11.3\,\mathrm{MW/m^3}$ presented in [3], which means a relative difference of about 50%. In general the results were affected by a relative difference higher than 10%, as shown in table 4.4.

Table 4.4: Average volumetric power deposition and total power deposition in each material layer in the ARC reactor using the response number MT=-4 (the results obtained with Serpent are provided with the absolute error)

	Vol. power $[\mathrm{MW/m^3}]$	Vol. power [3] $[\mathrm{MW/m^3}]$
First wall	19.228±0.006	24.1
Inner VV	16.776±0.003	11.3
Cooling channel	12.346±0.002	11.0
Neutron multiplier	5.668±0.001	6.3
Outer VV	8.367±0.001	7.4
FLiBe blanket	0.7459±0.0001	1.1
PF coil shielding	0.0015±0.0001	0.04

Since the results obtained for the average volumetric power deposition in the different components are not consistent with the ones found in the literature, we can expect that also the power deposition profiles will be not correct.

For this reason MT=-4 was substituted with MT=-80 defined more clearly as "total energy deposition with the combination of responses for fission heating, neutron heating based on KERMA coefficients and analog photon heating". However, in order to use this response function, it is necessary to introduce the photons in the transport simulation.

At this point, it is possible to evaluate the total power deposited by neutrons and photons in each component, defining a cell detector for each material layers. In this case the source rate normalization must be set to $1.86 \times 10^{20}\,\mathrm{neutrons/s}$, to take into account the power associated to the neutrons produced by D-T reactions in ARC ($420\,\mathrm{MW}$).

The average global results of volumetric power deposition inside the different components obtained with this first evaluation are presented in table 4.5 and compared with the ones of [3]. Considering the volumetric power deposition, the differences between the results obtained using Serpent and the ones presented by [3] are affected also by the difference in the volumes (table 3.1), in particular for what concerns the FLiBe blanket.

A better comparison can be done observing the total power deposited in the different layers. In this case, the differences related to the first wall, the inner vacuum vessel, the cooling channel, the neutron multiplier, the outer vacuum vessel and

Table 4.5: Average volumetric power deposition and total power deposition in each material layer in the ARC reactor (the results obtained with Serpent are provided with the absolute error)

	Vol. power $[\mathrm{MW/m^3}]$	Vol. power [3] $[\mathrm{MW/m^3}]$	Power [MW]	Power [3] [MW]
First wall	26.526 ± 0.008	24.1	8.488 ± 0.003	8.4
Inner VV	12.736 ± 0.002	11.3	41.646 ± 0.007	39.6
Cooling channel	13.043 ± 0.002	11.0	85.822 ± 0.012	77.7
Neutron multiplier	6.772 ± 0.001	6.3	22.415 ± 0.004	22.4
Outer VV	7.418 ± 0.001	7.4	74.328 ± 0.010	78.8
FLiBe blanket	0.7815 ± 0.0001	1.1	237.58 ± 0.03	255
PF coil shielding	0.0035 ± 0.0001	0.04	0.1523 ± 0.0006	1.8
Total			470.42 ± 0.06	484

the FLiBe blanket are under the 10%.

The huge difference in the power deposition in the poloidal field coil shielding is mainly due to the fact that it is located far from the plasma, so few neutrons are able to reach it and deposit power.

In order to obtain a better result in the neutron shielding we should increase the the total number of source neutrons run, but this would increase the simulation time. Considering that the power deposited in the coil shielding does not contribute to the electric power production (but it is mainly related to the magnet cooling) and that its contribution to the total power is negligible, the price to pay increasing the total number of source neutrons run or using some variance reduction technique is unmotivated in this study.

Finally, the total power deposited in the layers of the ARC reactor is comparable with the value of [3] (with a difference of 3%), representing another verification of the Serpent model used in this work.

The total power evaluated with Serpent ($470\,\mathrm{MW}$) is higher than the power associated to the neutrons generated inside the plasma ($420\,\mathrm{MW}$), mainly due to the exothermic reactions between neutrons and ^{6}Li. Actually there are also endothermic reactions between neutrons and ^{7}Li and also with fluorine, but they occur only whit fast neutrons, so their importance is smaller even if not negligible.

It is also interesting to make some considerations about the contribution of neutrons and photons in the different layers. The results obtained with Serpent are shown in table 4.6.

In general, the power deposited by photons is higher in denser materials (the first wall made of tungsten, the inner and outer vacuum vessels made of Inconel 718 and the PF coil shielding made of zirconium hydride) compared to the power deposited by neutrons mainly because the photon KERMA contribution is orders of magnitude lower in lighter materials (like lithium, fluorine and beryllium) and is

Table 4.6: Contribution of neutrons and photons to the average volumetric power deposition (results are provided with the absolute error)

	Neutrons volumetric power [MW/m^3]	Photons volumetric power [MW/m^3]
First wall	1.1616±0.0004	25.364±0.008
Inner VV	5.4268±0.0008	7.3087±0.0016
Cooling channel	11.683±0.002	1.3601±0.0004
Neutron multiplier	5.7161±0.0011	1.0559±0.0004
Outer VV	2.2547±0.0003	5.16330±0.0009
FLiBe blanket	0.6623±0.0001	0.1192±0.0001
PF coil shielding	0.00056557±0.000004	0.00293±0.00001

extremely high for tungsten.

On the other hand, the power deposition deposited by neutrons is higher in lighter media, since the KERMA coefficients in general are higher in lighter materials (in particular lithium, fluorine and beryllium) for fast neutrons (with energy between 1 MeV and 14.1 MeV) and in the vacuum vessel the fast spectrum is predominant (see fig. 4.3).

All the previous considerations have been made according to the cross section data provided by the JANIS (Java-based Nuclear Information Software) database of NEA (Nuclear Energy Agency), in particular considering MT=301 (KERMA total) and MT=442 (total photon KERMA contribution).

The results of table 4.6 are a demonstration of the fact that the addition of the photons in the the transport simulation of Serpent is fundamental in order not to underestimate the power deposition in the blanket of ARC.

However, even if the volumetric power deposition due to photons is higher in some layers (like the first wall and the inner and outer vacuum vessel), the contribution of neutrons on the total power deposited is predominant because most of the power is deposited in the FLibe cooling channel and in the FLiBe blanket. Table 4.7 represents the global contribution of neutrons and photons.

Table 4.7: Contribution of neutrons and photons to the total power deposition inside the blanket tank

	Neutrons	Photons	Total
Power [MW]	337.93±0.04	132.49±0.02	470.42±0.06

It is not sufficient to know the average global volumetric power deposited in each layer, but also some information regarding the spatial distribution of the power are necessary.

The first cylindrical detector is put in the equatorial region (Det1 in table 3.11) and the result is shown in fig. 4.8. Observing the plot, there is a central region that

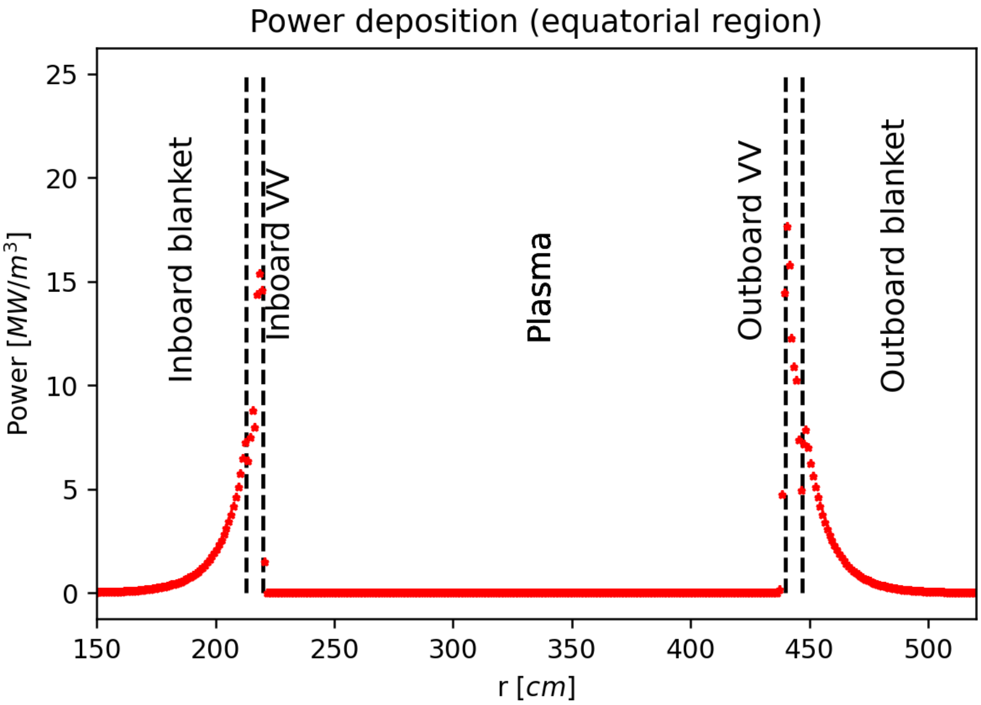

Figure 4.8: Radial volumetric power deposition in the equatorial region. The error bars are not visible because the scale is linear and, even if the relative error is high for the lowest and highest values of the radial coordinate, their influence on the final result is negligible because in these regions the power deposition is low compared to the values near the plasma.

coincides with the vacuum chamber where the deposited power vanishes and, again, two peaks inside the vacuum vessel. Then, the volumetric power decreases exponentially as expected. The two peaks correspond to volumetric power densities in the order of 15-20 $\mathrm{MW/m^3}$.

The plot in fig. 4.8 does not provide enough detail about the region between the first wall and the outer vacuum vessel, which is probably the most important in the reactor because composed of many different materials.

Figure 4.9 represents the detail of this part of ARC. In both the plots there is a peak in correspondence of the first wall, confirming the result in table 3.11. Then the power decreases in the inner vacuum vessel and increases again in the cooling channel where it is almost constant. After a sudden drop in the neutron multiplier, the power deposition is higher in the outer vacuum vessel and finally decays exponentially in the FLiBe blanket.

These results demonstrate that a significant amount of power is absorbed by the inner and outer vacuum vessels. According to this conclusion, it is clear how much important is to remove the power deposited in the vacuum vessel in order maintain its structural role.

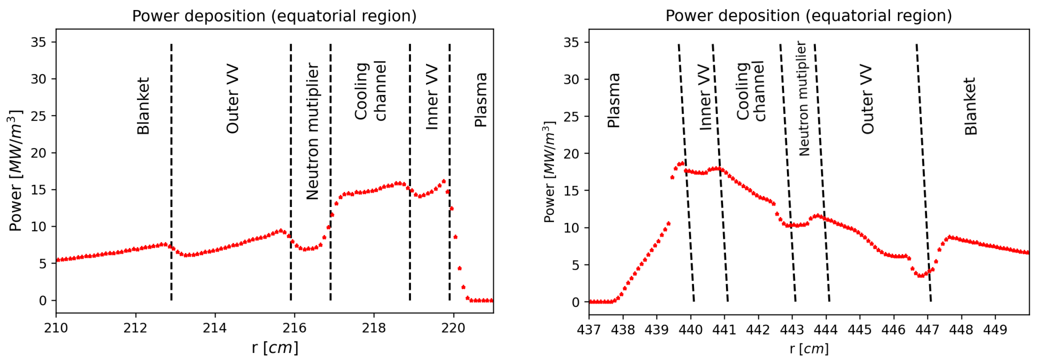

(a) *Volumetric power deposition (inboard)* **(b)** *Volumetric power deposition (outboard)*

Figure 4.9: Radial power deposition in the equatorial region on the inboard (a) and outboard (b) side of the vacuum vessel. The error bars are not visible because the relative error is too low.

From the power deposition profiles and knowing the maximum allowable temperature of Inconel 718, it is possible to evaluate the mass flow rate of FLiBe requested in order to guarantee the structural integrity of the inner and outer vacuum vessels.

This plot underlines also the importance of having a more detailed information about the power deposition instead of a single global one: for example the average result of the inner vacuum vessel in table 4.5 is $12.736\,\mathrm{MW/m^3}$, but observing the plot the highest value of power deposition of the inner vacuum vessel at the midplane of the reactor is about $17\,\mathrm{MW/m^3}$. Therefore, it is possible that considering the average result the structural integrity of the vacuum vessel is guaranteed, but this is actually not true because maybe in some localized region the power deposition is higher than the limits associated to the material.

Another cylindrical detector for the evaluation of the power deposition is put immediately below the upper divertor leg (Det4 in table 3.11). The corresponding radial profile is represented in fig. 4.10. The shape of the spatial distribution is similar to the equatorial one, obviously the central part with zero power deposition is smaller because here the vacuum chamber is smaller. The amplitude of the plots are similar too, because the neutron source is spatially uniform.

Also in this case, it is interesting to analyse in further detail the power distribution inside the vacuum vessel, as shown in fig. 4.11 The power deposition distribution on the inboard side has a similar shape and amplitude to the one in the equatorial region. On the outboard side the plot is not characterized by any drop because in this region the reactor has a strong curvature, so it is impossible to detect the power deposition of each single material for any single radial value.

Finally, the volumetric power deposition in the blanket above the divertor region (fig. 4.12) is even smaller, as expected. The peak is located in the proximity of the divertor again.

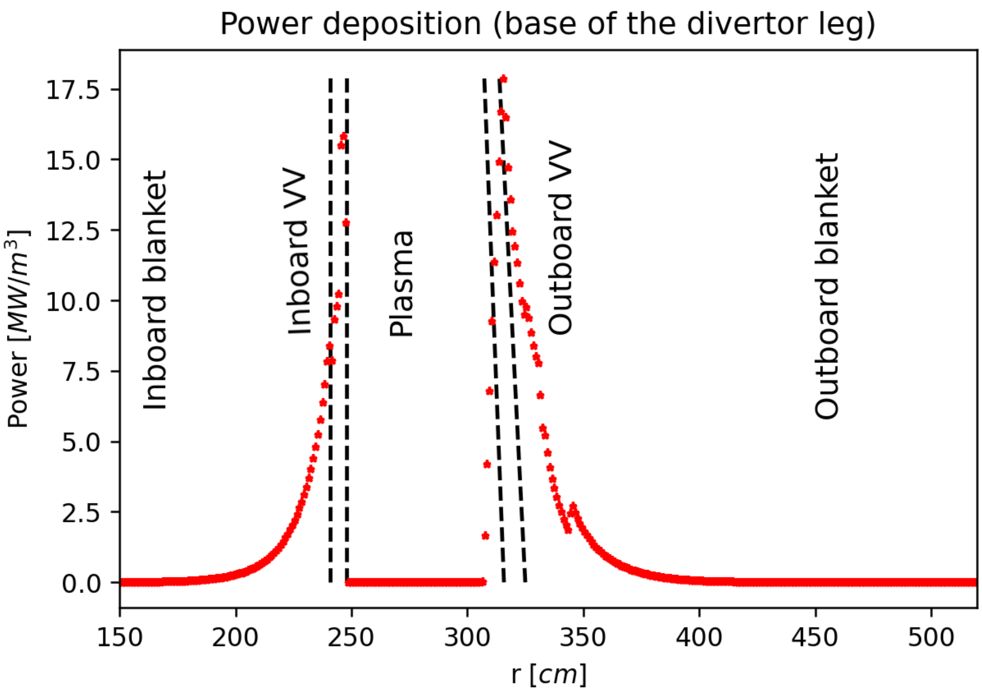

Figure 4.10: Radial volumetric power deposition at the base of the upper divertor leg. The error bars are not visible because the scale is linear and, even if the relative error is high for the lowest and highest values of the radial coordinate, their influence on the final result is negligible because in these regions the power deposition is low compared to the values near the plasma.

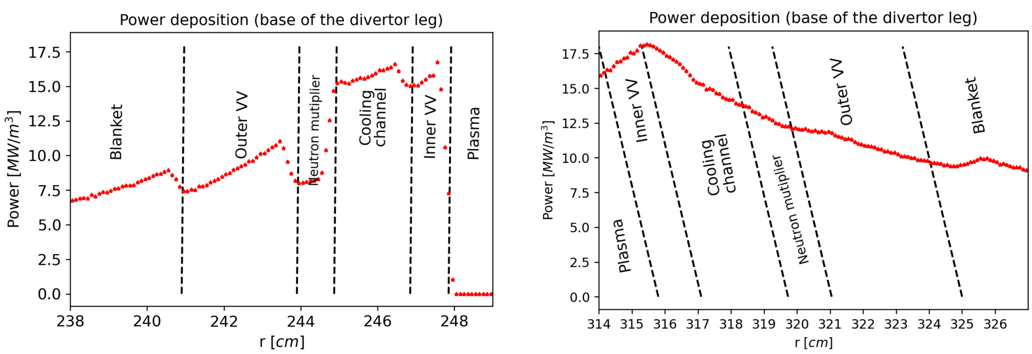

(a) *Volumetric power deposition (inboard)* **(b)** *Volumetric power deposition (outboard)*

Figure 4.11: Radial power deposition at the base of the upper divertor leg on the inboard (a) and outboard (b) side of the vacuum vessel.The error bars are not visible because the relative error is too low.

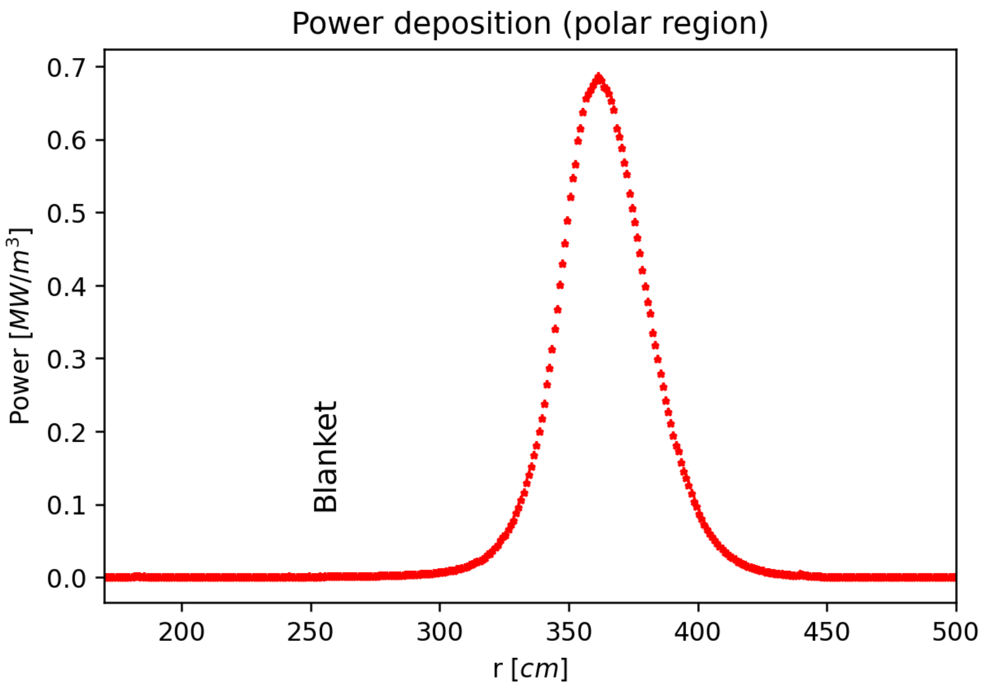

Figure 4.12: Radial volumetric power deposition above the upper divertor. The error bars are not visible because the scale is linear and, even if the relative error is high for the lowest and highest values of the radial coordinate, their influence on the final result is negligible because in these regions the power deposition is low compared to the values near the plasma.

4.2 Non-uniform source

The next step after the first evaluation with the spatially uniform source, is to perform a set of simulations with the non-uniform source. The results obtained with Serpent are focused on the neutron flux (subsection 4.2.1) , the tritium breeding ratio (subsection 4.2.2) and the power deposition (subsection 4.2.3).

The input files used for the Serpent simulations with the non-uniform source can be found at [26].

4.2.1 Neutron flux

According to the results presented in section 4.1, even with a spatially uniform source of neutrons inside the plasma chamber, the quantities estimated using Serpent are comparable with the ones found in the literature. However, one of the aim of this work is to try to obtain more realistic results too, by considering a first approximation of a non-uniform source.

A first possible improvement is the use of a non-uniform source as the one described in chapter 3.4, defining a series of toroidal sources each one with a different weight.

The neutron flux evaluated on the whole blanket (in fig. 4.13) is similar to the one obtained with the spatially uniform source (fig. 4.1), the main difference is that in the former the peak coincident with the centre of the plasma at 330 cm is more pronounced in the linear plot, since the neutron emission profile is no longer uniform in the plasma chamber but has a maximum at the centre, where the plasma density and the plasma temperature are the highest.

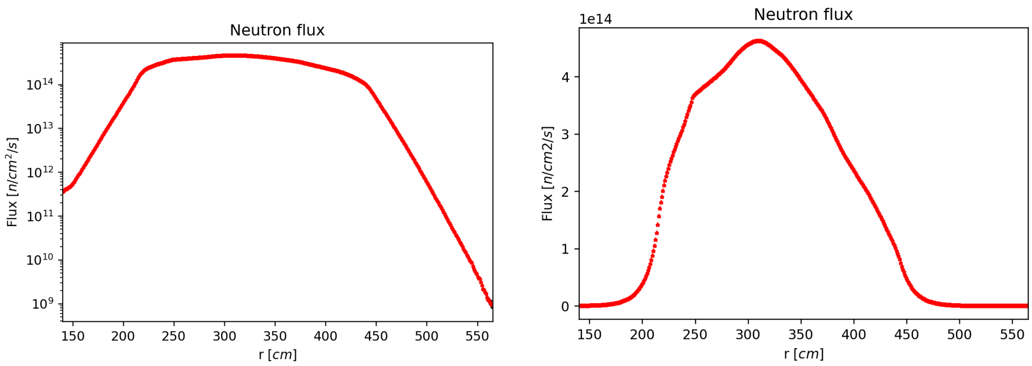

(a) *Radial neutron flux (logarithmic scale)* **(b)** *Radial neutron flux (linear scale)*

Figure 4.13: Radial neutron flux in the whole breeding blanket tank in logarithmic (a) and linear (b) scale. The error bars are not visible because the relative error is too low.

In this case too, as expected, the neutron flux decays exponentially in the breeding blanket because it is not a multiplying material.

The neutron flux distributions at different heights with the non-uniform source are shown in fig. 4.14. In fig. 4.14 (b) it is clear how the flux is not constant in the region corresponding with the plasma chamber, because now we are considering a non-uniform source where the neutron emission is higher in the main plasma at the centre of the chamber. Thus, the result of the neutron flux in the equatorial region is consistent with the source definition.

Far from the main plasma, at the base of the upper divertor leg, the neutron flux is smaller than the one at the mid-plane. This is an improvement and a more realistic result compared to the spatially uniform source where the neutron flux at the mid-plane had similar values to the ones at the base of the divertor leg.

Again, the neutron flux in the polar region above the divertor (fig. 4.14 (e), (f)) is about two order of magnitudes lower than the neutron flux at the mid-plane and at the base of the divertor leg.

For what concerns the neutron spectrum, there are no particular differences bewteen the results obtained with the spatially uniform and the non-uniform source.

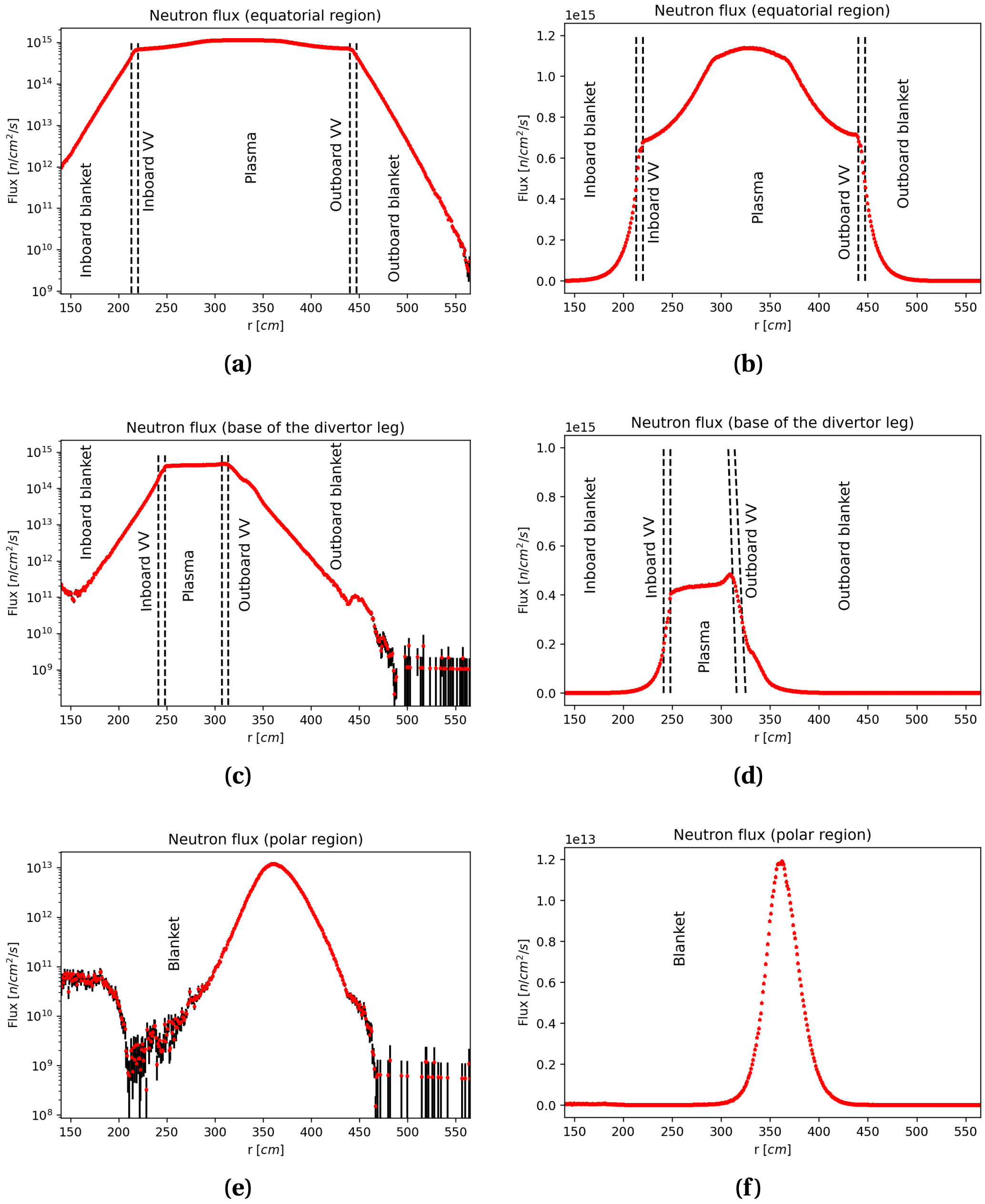

Figure 4.14: Neutron flux in the equatorial region (a) (b), at the base of the upper divertor leg (c) (d) and above the upper divertor (e) (f), in logarithmic (left column) and linear (right column) scale. The error bars are visible in the logarithmic plots.

4.2.2 Tritium breeding ratio

The global TBR, evaluated with the non-uniform source, is equal to 1.0853, with a contribution of about 23% from the cooling channel and the remaining 77% from the breeding blanket (table 4.8).

Table 4.8: Global values ot TBR

Total	Cooling channel	Blanket
1.0853±0.0002	0.2526±0.0001	0.8303±0.0001

Concerning the radial distribution of the reaction rate of neutrons with lithium for the tritium production inside ARC at the mid-plane, the result is shown in fig. 4.15. The non-uniform source does not modify the shape of the distribution of

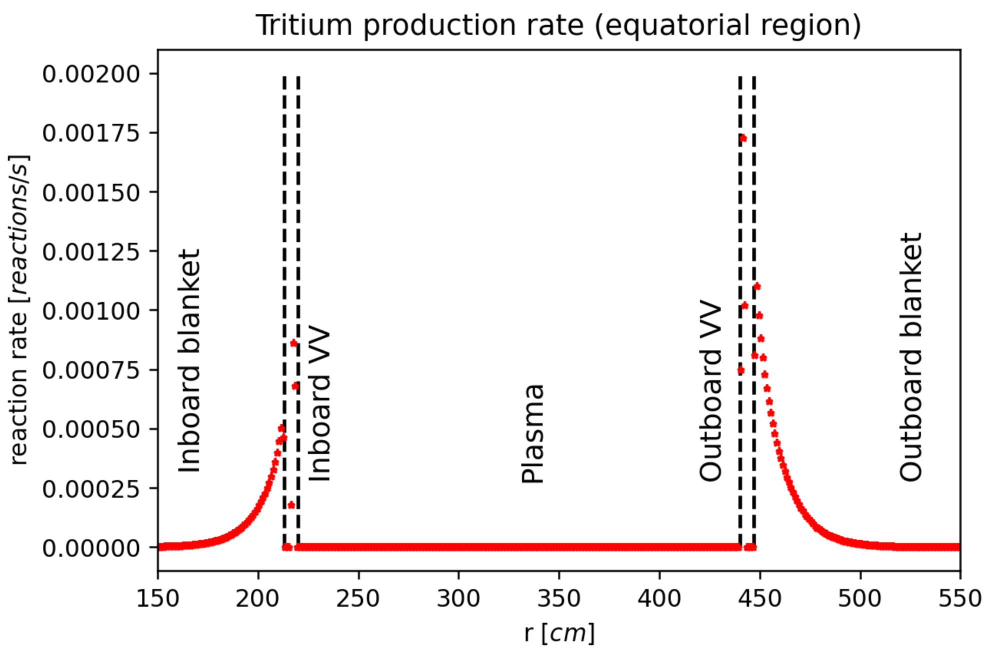

Figure 4.15: Radial distribution of the reaction rate in the equatorial region. The error bars are not visible because the scale is linear and, even if the relative error is high for the lowest and highest values of the radial coordinate, their influence on the final result is negligible because in these regions the reaction rate is low compared to the values near the plasma.

the reaction rate, with the characteristic peaks coincident with the cooling channel and the exponential decay in the breeding blanket. Obviously, the reaction rate is still zero in the plasma chamber.

Again, the contribution of ^{6}Li is much higher than the one of ^{7}Li (fig. 4.16).

Figure 4.17 and fig. 4.18 show, respectively, the reaction rate of neutrons and lithium at the base of the divertor leg and above the upper divertor. In fig. 4.17, the values associated to the reaction rate are lower than the corresponding values at the mid-plane, confirming the results already found for the neutron flux using a non-uniform source.

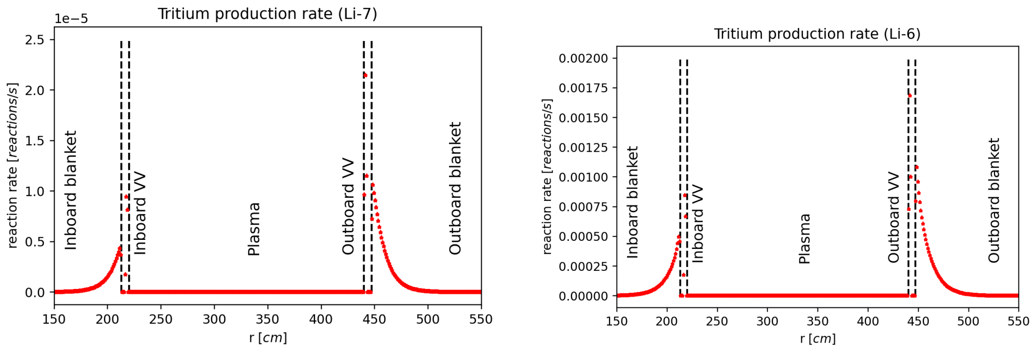

(a) *Radial reaction rate relative to* ^{7}*Li* **(b)** *Radial reaction rate relative to* ^{6}*Li*

Figure 4.16: Radial distribution of the reaction rate relative to ^{7}Li (a) and to ^{6}Li (b) in the equatorial region. The error bars are not visible because the scale is linear and, even if the relative error is high for the lowest and highest values of the radial coordinate, their influence on the final result is negligible because in these regions the reaction rate is low compared to the values near the plasma.

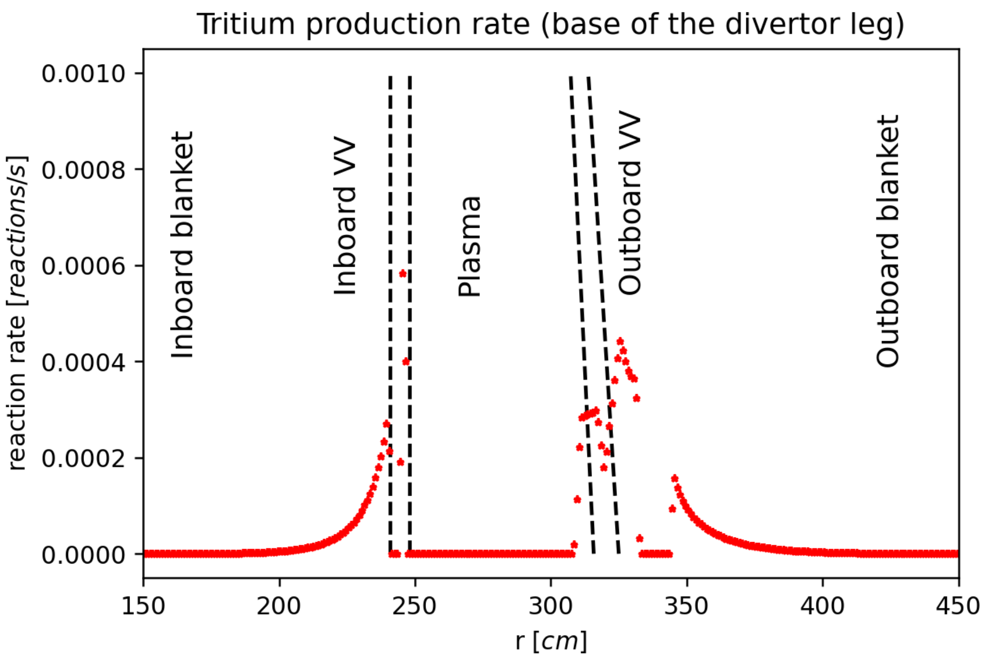

Figure 4.17: Radial distribution of the reaction rate at the base of the upper divertor leg. The error bars are not visible because the scale is linear and, even if the relative error is high for the lowest and highest values of the radial coordinate, their influence on the final result is negligible because in these regions the reaction rate is low compared to the values near the plasma.

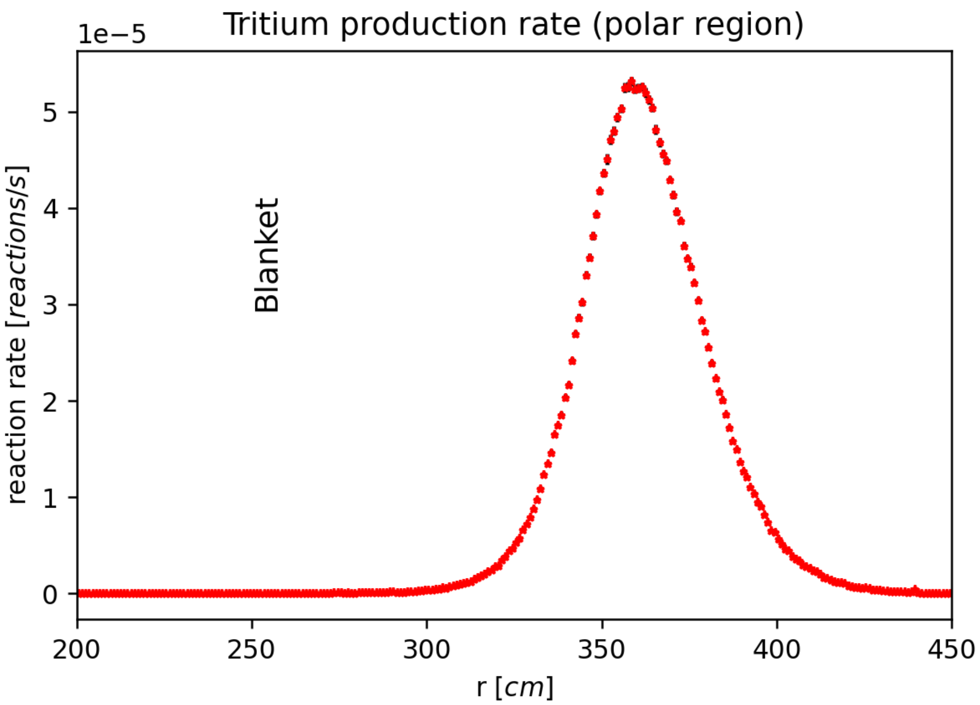

Figure 4.18: Radial distribution of the reaction rate in the blanket above the upper divertor. The error bars are not visible because the scale is linear and, even if the relative error is high for the lowest and highest values of the radial coordinate, their influence on the final result is negligible because in these regions the reaction rate is low compared to the values near the plasma.

The reaction rate above the upper divertor is small, since few neutrons manage to arrive in this region. In particular it is smaller than the reaction rate in the polar region evaluated with a spatially uniform source (fig. 4.7), because in the latter case we supposed that the probability to generate a neutron near the divertor was the same to the probability at the mid-plane, so there were more neutrons in that part of the plasma able to reach the polar region of the breeding blanket.

4.2.3 Volumetric power deposition

The average volumetric power deposited by neutrons and photons in each component, associated to the non-uniform source, is shown in table 4.9. The main difference in this case is that the average volumetric power depositions are smaller than the ones estimated with the spatially uniform source (table 4.5) inside the vacuum vessel while it is higher in the breeding blanket.

These two effects compensate and the result is a total deposited power of $472\,\mathrm{MW}$, comparable with the $470\,\mathrm{MW}$ of the spatially uniform source, higher than the fusion power $(420\,\mathrm{MW})$ mainly because of exothermic reactions with ^{6}Li.

Table 4.9: Average volumetric power deposition and total power deposition in each material layer in the ARC reactor (the results obtained with Serpent are provided with the absolute error)

	Vol. power [MW/m^3]	Vol. power [3] [MW/m^3]	Power [MW]	Power [3] [MW]
First wall	23.165±0.007	24.1	7.4128±0.0023	8.4
Inner VV	10.908±0.002	11.3	35.669±0.006	39.6
Cooling channel	12.0197±0.002	11.0	79.090±0.010	77.7
Neutron multiplier	6.5262±0.0013	6.3	21.602±0.004	22.4
Outer VV	7.3179±0.0011	7.4	73.325±0.011	78.8
FLiBe blanket	0.83884±0.00084	1.1	255.02±0.03	255.0
PF coil shielding	0.00277±0.00001	0.04	0.12050±0.0005	1.8
Total			472.24±0.06	484

Also in this case it is possible to evaluate the power deposition profiles and compare them to the results obtained in subsection 4.1.3.

The radial distribution of the power deposition at the mid-plane are shown in fig. 4.19 and fig. 4.20. In this case, the power deposited at the mid-plane is higher than the values obtained in the spatially uniform case (fig. 4.8 and 4.9) because now the neutron source is localized in the central region of the plasma chamber.

The radial profile of the volumetric power deposition at the base of the upper divertor leg is represented in fig. 4.21 and fig. 4.22. Again, the shape of the power deposition is similar to the equatorial one but the amplitude is in general lower, consistently with the non-uniform source definition.

Finally, the volumetric power deposition in the blanket above the divertor region (fig. 4.23) is smaller compared to the previous volumetric powers. The peak is located in the proximity of the divertor again.

In conclusion, the results obtained with the non-uniform source are comparable to the ones obtained with the spatially uniform source. In both cases they are consistent with other results presented in the literature [3].

Since it has proven that Serpent gives good results for the estimation of quantities like the TBR and the power deposition using two simple types of source, the next step could be to define a more realistic neutron source with a continuous distribution in the whole volume of the plasma chamber and not based on average weights with a sort of step-wise distribution limited to the central region of the plasma, as described in chapter 3.4.

A possible solution in this sense could be the use of the "df" card provided by Serpent which allows to use a pre-generated file for the definition of the source distribution, giving as input the cartesian coordinates, direction cosines, weights and energies of the source points.

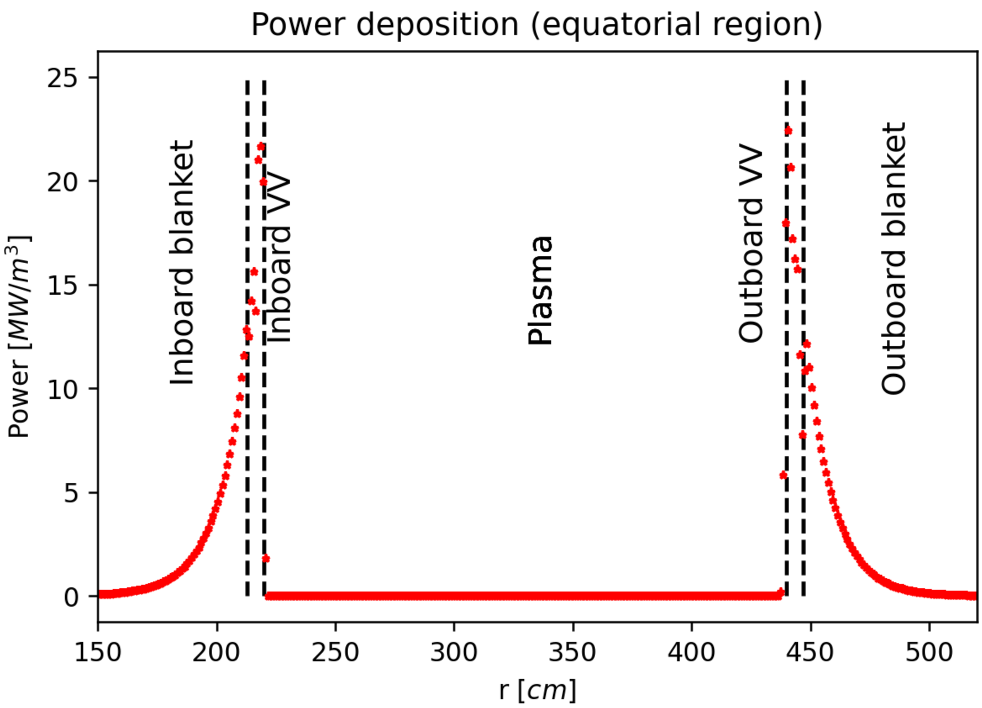

Figure 4.19: Radial volumetric power deposition in the equatorial region. The error bars are not visible because the scale is linear and, even if the relative error is high for the lowest and highest values of the radial coordinate, their influence on the final result is negligible because in these regions the power deposition is low compared to the values near the plasma.

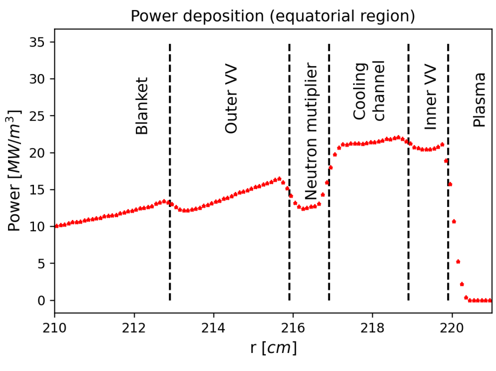

(a) *Volumetric power deposition (inboard)*

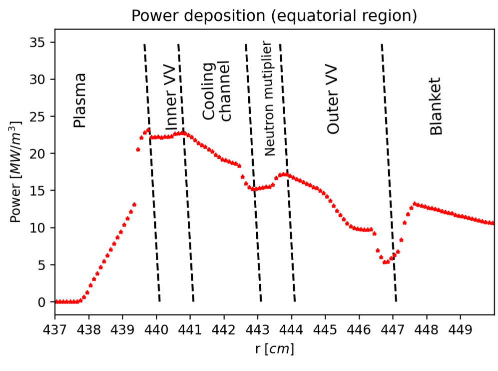

(b) *Volumetric power deposition (outboard)*

Figure 4.20: Radial power deposition in the equatorial region on the inboard (a) and outboard (b) side of the vacuum vessel.The error bars are not visible because the relative error is too low.

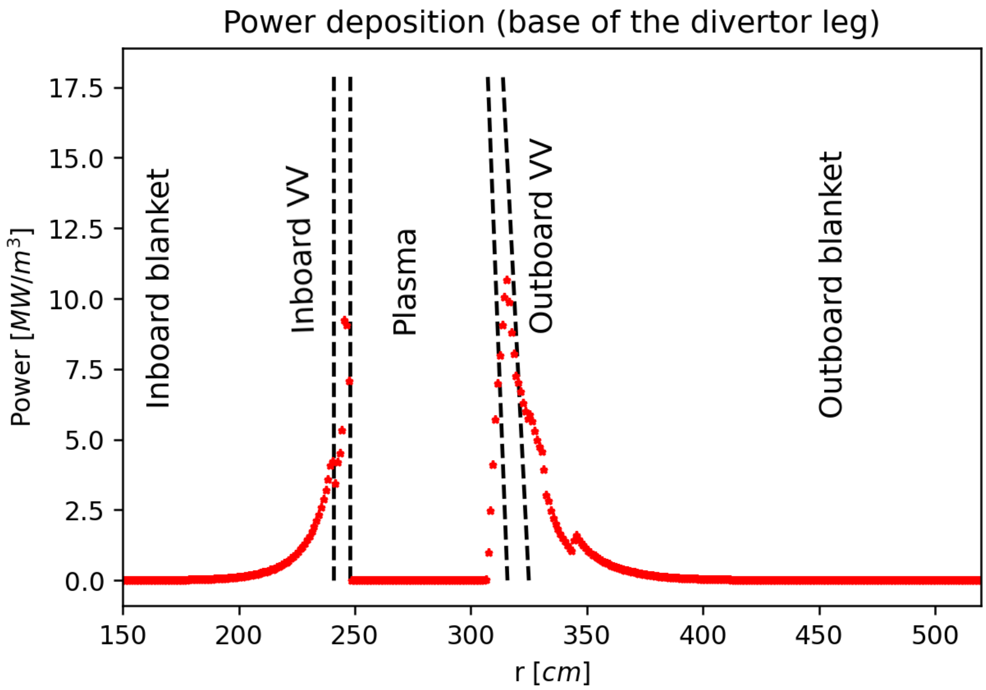

Figure 4.21: Radial volumetric power deposition at the base of the upper divertor leg. The error bars are not visible because the scale is linear and, even if the relative error is high for the lowest and highest values of the radial coordinate, their influence on the final result is negligible because in these regions the power deposition is low compared to the values near the plasma.

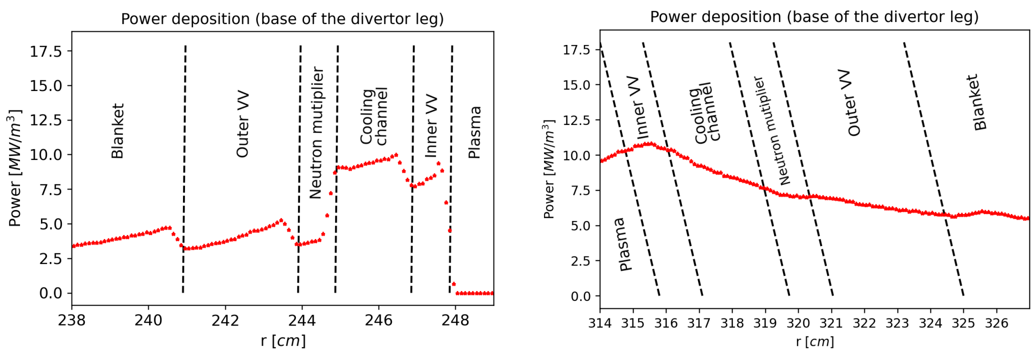

(a) *Volumetric power deposition (inboard)* **(b)** *Volumetric power deposition (outboard)*

Figure 4.22: Radial power deposition at the base of the upper divertor leg on the inboard (a) and outboard (b) side of the vacuum vessel. The error bars are not visible because the relative error is too low.

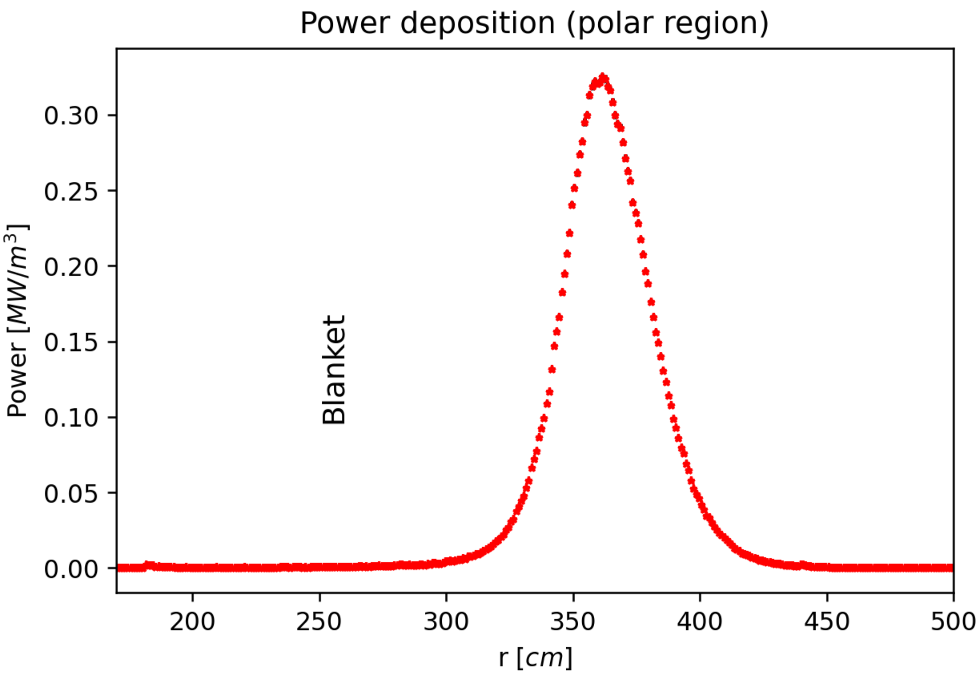

Figure 4.23: Radial volumetric power deposition above the upper divertor. The error bars are not visible because the scale is linear and, even if the relative error is high for the lowest and highest values of the radial coordinate, their influence on the final result is negligible because in these regions the power deposition is low compared to the values near the plasma.

Chapter 5

Conclusions and future perspectives

The Monte Carlo modelling of the ARC reactor was performed using the Monte Carlo transport code Serpent. The simulations were focused on an integral quantity like the tritium breeding ratio (TBR), fundamental for the fuel self-sustainment of the reactor, and on the power deposited both by neutrons and photons, that guarantees the production of electrical power.

In the past, Serpent was mainly used for the modelling of fission reactors, but with the introduction of the external source mode it became suitable, in principle, also for non-multiplying devices like fusion reactors.

Serpent allows to define simple surfaces and lattices which are particularly suitable for fission systems. In the case of fusion reactors, it is not possible to directly use Serpent for the definition of its geometry. For this reason the geometry model of ARC was developed on Solidworks and then imported in Serpent using the STL format.

However, the main limitation of Serpent for applications in fusion devices is related to the source definition. In fission devices the neutron external source distribution in the phase space (if present) is usually quite simple, therefore Serpent is not very flexible with the definition of more complex sources. In a fusion reactor the neutron source is complex and depends on the plasma physics, so Serpent could be not the best choice in this sense. It allows to define spatially uniform sources, which are not realistic but allow to obtain a first approximation of the neutronics in ARC, as shown in section 4.1.

In order to obtain more realistic sources it is possible to exploit some surface types embedded in Serpent, like toroidal surfaces, and to assign to each of these surfaces a source with a different weight. In this way the source is no more spatially uniform but there is a higher probability to generate a neutron at the centre of the plasma chamber than at the plasma edge, consistently with the plasma physics. The results obtained with this source are presented in section 4.2.

Either detectors for the evaluation of integral quantities and for distributions in space were defined. In particular the result obtained for the global TBR shows that the design of ARC is able to produce an amount of tritium higher than the burnt one in the plasma.

The results estimated using Serpent are consistent with the ones that can be found in the literature for ARC, where usually the code employed was MCNP. This is an important result because it justifies the use of Serpent for the neutronics modelling of other fusion reactors in the future and also the further employment of Serpent for more detailed works on ARC.

Using a population of 10^8 neutrons the statistical error is usually negligible, except for detectors located in regions far from the neutron source. However, in this case, the evaluated quantities are so low that the influence of the statistical error is negligible on the final result.

It is clear that the neutron sources used in this work are not consistent with the plasma physics, therefore a source where the probability of generating a neutron is different at any point of the plasma chamber should be defined. A solution of this type requires a better knowledge of the plasma physics in ARC and could be a possible improvement for future work.

Another aspect that should be improved in Serpent is the fact that the detectors that can be defined are good in the case of simple, elementary geometries (like the fuel rods of a fission reactor) but have some limitations in complex geometries like fusion reactors.

The definition of a more precise neutron source is not the only aspect that should be taken into account for future works on ARC.

Other possible fields of study are, for example, the coupling of the neutronics results with 3D MHD/CFD models for the evaluation of the FLiBe flow and pressure drops in the blanket and of the power extraction.

Since the production of tritium is due to the interaction of neutrons with lithium, more reliable results could be obtained performing an uncertainty quantification on nuclear data associated with lithium, since this is a material usually not present in fission reactors, therefore its nuclear data could be affected by a relatively large uncertainty.

Finally, it should be important to improve the ARC Serpent modelling of the neutron shielding, using variance reduction techniques in order to cope with the issue of the low statistics in regions far from the neutron source.

Bibliography

[1] B.N. Sorbom, J. Ball, T.R. Palmer, F.J. Mangiarotti, J.M. Sierchio, P. Bonoli, C. Kasten, D.A. Sutherland, H.S. Barnard, C.B. Haakonsen, J. Goh, C. Sung, and D.G. Whyte. «ARC: A compact, high-field, fusion nuclear science facility and demonstration power plant with demountable magnets». In: *Fusion Engineering and Design* 100 (2015), pp. 378–405.

[2] S. Segantin, R. Testoni, and M. Zucchetti. «The lifetime determination of ARC reactor as a load-following plant in the energy framework». In: *Energy policy* 126 (2019), pp. 66–75.

[3] A.Q. Kuang, N.M. Cao, A.J. Creely, C.A. Dennett, J. Hecla, B. LaBombard, R.A. Tinguely, E.A. Tolman, H. Hoffman, M. Major, J. Ruiz Ruiz, D. Brunner, P. Grover, C. Laughman, B.N. Sorbom, and D.G. Whyte. «Conceptual design study for heat exhaust management in the ARC fusion pilot plant». In: *Fusion Engineering and Design* 137 (2018), pp. 221–242.

[4] M. V. Umansky, B. LaBombard, D. Brunner, M. E. Rensink, T. D. Rognlien, J. L. Terry, and D. G. Whyte. «Attainment of a stable, fully detached plasma state in innovative divertor configurations». In: *Physics of Plasmas* 24 (2017).

[5] T. Eich, A.W. Leonard, R.A. Pitts, W. Fundamenski, R.J. Goldston, T.K. Gray, A. Herrmann, A. Kirk, A. Kallenbach, O. Kardaun, A.S. Kukushkin, B. LaBombard, R. Maingi, M.A. Makowski, A. Scarabosio, B. Sieglin, J. Terry, A. Thornton, ASDEX Upgrade Team, and JET EFDA Contributors. «Scaling of the tokamak near the scrape-off layer H-mode power width and implications for ITER». In: *Nuclear Fusion* 53 (2013).

[6] M.L. Reinke. «Heat flux mitigation by impurity seeding in high-field tokamaks». In: *Nuclear Fusion* 57 (2017).

[7] T. Shi, H. Li, Q. Ding, M. Wang, Z. Zheng, C. Peng, and Q. Mei. «Global variance reduction method based on multi-group Monte Carlo adjoint calculation». In: *Annals of Nuclear Energy* 151 (2021).

[8] J. Leppänen, M. Pusa, Viitanen T, V. Valtavirta, and T. Kaltiaisenaho. «The Serpent Monte Carlo code: Status, development and applications in 2013». In: *Annals of Nuclear Energy* 82 (2013), pp. 142–150.

[9] E. R. Woodcock, T. Murphy, P. J. Hemmings, and T. C. Longworth. «Techniques used in the GEM code for Monte Carlo neutronics, calculations in reactors and other systems of complex geometry». In: *Proc. Conf. Applications of Computing Methods to Reactor Problems.* Vol. 557. 2. 1965.

[10] J. Leppänen. «On the use of delta-tracking and the collision flux estimator in the Serpent 2 Monte Carlo particle transport code». In: *Annals of Nuclear Energy* 105 (2017), pp. 161–167.

[11] J. Leppänen. «Performance of Woodcock delta-tracking in lattice physics applications using the Serpent Monte Carlo reactor physics burnup calculation code». In: *Annals of Nuclear Energy* 37 (2010), pp. 715–722.

[12] J. Leppänen, ed. *CAD-Based Geometry Type in Serpent 2: Application in Fusion Neutronics.* Cambridge, UK, July 2015.

[13] S. Segantin, R. Testoni, Z. Hartwig, D. Whyte, and M. Zucchetti. «Optimization of tritium breeding ratio in ARC reactor». In: *Fusion Engineering and Design* 154 (2020).

[14] A. Thomas, M. El-Wahabi, J.M. Cabrera, and J.M. Prado. «High temperature deformation of Inconel 718». In: *Journal of Materials Processing Technology* 177 (2006), pp. 469–472.

[15] B. Bocci, Z. Hartwig, S. Segantin, R. Testoni, D. Whyte, and M. Zucchetti. «ARC reactor materials: Activation analysis and optimization». In: *Fusion Engineering and Design* 154 (2020).

[16] P. Tolias and the EUROfusion MST1 Team. «Analytical expressions for thermophysical properties of solid and liquid tungsten relevant for fusion applications». In: *Nuclear Materials and Energy* 13 (2017), pp. 42–57.

[17] H. Hosaeus, A. Seifter, E. Kaschnitz, and G. Pottlacher. «Thermophysical properties of solid and liquid Inconel 718 alloy». In: *High Temperatures - High Pressures* 33 (2001).

[18] R. Serrano-López, J. Fradera, and S. Cuesta-López. «Molten salts database for energy applications». In: *Chemical Engineering and Processing: Process Intensification* 73 (2013), pp. 87–102.

[19] C. Forsberg, G. Zheng, R. G. Ballinger, and S. T. Lam. «Fusion Blankets and Fluoride-Salt-Cooled High-Temperature Reactors with Flibe Salt Coolant: Common Challenges, Tritium Control, and Opportunities for Synergistic Development Strategies Between Fission, Fusion, and Solar Salt Technologies». In: *Nuclear Technology* (2019).

[20] A. Jolodosky, M. Aufiero, and M. Fratoni. «Exact perturbation theory for fusion blanket design». In: *Annals of Nuclear Energy* 131 (2019), pp. 353–366.

[21] Y. Lu, G. Zhou, F. A. Hernández, P. Pereslavtsev, J. Leppänen, and M. Ye. «Benchmark of Serpent-2 with MCNP: Application to European DEMO HCPB breeding blanket». In: *Fusion Engineering and Design* 155 (2020).

[22] A. Turner, A. Burns, B. Colling, and J. Leppänen. «Applications of Serpent 2 Monte Carlo Code to ITER Neutronics Analysis». In: *Fusion Science and Technology* 74 (2018), pp. 315–320.

[23] P. Sirén, J. Varje, S. Äkäslompolo, O. Asunta, C. Giroud, T. Kurki-Suonio, and H. Weisen. «Versatile fusion source integrator AFSI for fast ion and neutron studies in fusion devices». In: *Nuclear Fusion* 58.1 (2017), pp. 16–23.

[24] J.D. Huba. *NRL plasma formulary*. The Office of Naval Research. Washington, DC 20375, 2002.

[25] R. Tuominen, V. Valtavirta, and J. Leppänen. «New energy deposition treatment in the Serpent 2 Monte Carlo transport code». In: *Annals of Nuclear Energy* 129 (Feb. 2019), pp. 224–232.

[26] A. Aimetta. *Neutronic analysis of the fusion reactor ARC: Monte Carlo simulations with the Serpent code*. Nov. 2020. DOI: 10.5281/zenodo.4292229. URL: https://doi.org/10.5281/zenodo.4292229.